

SPITZER INFRARED LOW-RESOLUTION SPECTROSCOPIC STUDY OF BURIED AGNS IN A COMPLETE SAMPLE OF NEARBY ULTRALUMINOUS INFRARED GALAXIES

MASATOSHI IMANISHI¹

National Astronomical Observatory, 2-21-1, Osawa, Mitaka, Tokyo 181-8588, Japan

ROBERTO MAIOLINO

INAF - Osservatorio Astronomico di Roma, via di Frascati 33, I-00040 Monte Porzio Catone, Roma, Italy

AND

TAKAO NAKAGAWA

Institute of Space and Astronautical Science, Japan Aerospace Exploration Agency, 3-1-1 Yoshinodai, Sagami-hara, Kanagawa 229-8510, Japan

Astrophysical Journal

ABSTRACT

We present the results of *Spitzer* IRS low-resolution infrared 5–35 μm spectroscopy of 17 nearby ULIRGs at $z < 0.2$, optically classified as non-Seyferts. The presence of optically elusive, but intrinsically luminous, buried AGNs is investigated, based on the strengths of polycyclic aromatic hydrocarbon emission and silicate dust absorption features detected in the spectra. The signatures of luminous buried AGNs, whose intrinsic luminosities range up to $\sim 10^{12}L_{\odot}$, are found in eight sources. We combine these results with those of our previous research to investigate the energy function of buried AGNs in a complete sample of optically non-Seyfert ULIRGs in the local universe at $z < 0.3$ (85 sources). We confirm a trend that we previously discovered: that buried AGNs are more common in galaxies with higher infrared luminosities. Because optical Seyferts also show a similar trend, we argue more generally that the energetic importance of AGNs is intrinsically higher in more luminous galaxies, suggesting that the AGN-starburst connections are luminosity-dependent. This may be related to the stronger AGN feedback scenario in currently more massive galaxy systems, as a possible origin of the galaxy downsizing phenomenon.

Subject headings: galaxies: active — galaxies: ISM — galaxies: nuclei — galaxies: Seyfert — galaxies: starburst — infrared: galaxies

1. INTRODUCTION

Ultraluminous infrared galaxies (ULIRGs) are characterized by a spectral energy distribution dominated by infrared emission, and an absolute infrared luminosity with $L_{\text{IR}} > 10^{12}L_{\odot}$ (Sanders et al. 1988a; Sanders & Mirabel 1996). This means that in ULIRGs, (1) very luminous energy sources with $L > 10^{12}L_{\odot}$ are present, (2) the energy sources are hidden by dust, which absorbs most of the primary radiation, and (3) the heated dust grains then radiate this energy as infrared dust emission. The dust-obscured energy sources are nuclear fusion occurring inside rapidly formed stars (starbursts) and/or the release of gravitational energy generated by spatially compact, mass-accreting, supermassive black holes (SMBHs) (i.e., AGN activity). Because the ULIRG population becomes very important at $z > 1$, in terms of cosmic infrared radiation density (Caputi et al. 2007), understanding the hidden energy sources of ULIRGs is closely coupled with clarifying the connection between star formation and SMBH growth in the dust-obscured galaxy population of the early universe. Because distant ULIRGs are generally faint, detailed studies of nearby ($z < 0.3$) ULIRGs continue to play an important role in understanding the nature of the ULIRG population of the universe.

Nearby ULIRGs have two important observational properties. First, the fraction of optical Seyferts (optically identified AGNs) is known to be substantially greater in ULIRGs, compared with galaxies with lower infrared luminosities ($L_{\text{IR}} < 10^{12}L_{\odot}$) (Veilleux et al. 1999; Goto 2005). Second, although galaxies with $L_{\text{IR}} < 10^{12}L_{\odot}$ generally exhibit strong, spatially extended infrared emission originating from stars distributed inside them, the infrared dust emission of nearby ULIRGs is dominated by a spatially compact feature (Soifer et al. 2000, 2001), suggesting that a large amount of dust is concentrated in the nuclear regions of ULIRGs, and heated by spatially compact energy sources.

Because the nuclear dust concentration increases in ULIRGs (Sanders & Mirabel 1996; Soifer et al. 2000), the putative AGNs in ULIRG's cores are surrounded by a large amount of gas and dust, and ionizing UV radiation from the AGN can be blocked at the inner part (< 10 pc) in virtually all lines-of-sight (Hopkins et al. 2005; Imanishi et al. 2006, 2007). Such *buried* AGNs lack well-developed narrow-line-regions (NLRs) at 10–1000 pc scale, the primary sources of forbidden emission lines, and so are elusive through the conventional optical and infrared spectroscopic classification, looking for high-excitation forbidden emission lines from the NLRs (Veilleux & Osterbrock 1987; Kewley et al. 2006; Armus et al. 2007; Farrah et al. 2007). Low-resolution infrared 2.5–35 μm spectroscopy is an effective tool for studying

Electronic address: masa.imanishi@nao.ac.jp

¹ Department of Astronomy, School of Science, Graduate University for Advanced Studies, Mitaka, Tokyo 181-8588

such elusive (Maiolino et al. 2003) buried AGNs, for the following reasons. First, the effects of dust extinction are sufficiently small ($<0.06A_V$; Nishiyama et al. 2008; 2009) that buried AGNs are detectable. Second, in a normal starburst with moderate metallicity (>0.3 solar), consisting of UV-emitting HII regions, molecular gas and dust, and photo-dissociation regions (PDRs), the PAHs in the PDRs are excited by far-UV photons from stars without being destroyed, so strong PAH emission is usually detected (Sellgren 1981; Wu et al. 2006). However, PAHs in close proximity to an AGN are destroyed by the high-energy X-ray radiation of the AGN (Voit 1992), so that PAH emission is virtually absent from a pure AGN, as demonstrated from observations (Moorwood 1986; Roche et al. 1991; Genzel et al. 1998; Imanishi & Dudley 2000). In a galaxy hosting an AGN, strong PAH emission can be observed, if PAHs survive in the regions shielded from the high-energy radiation of the AGN, and PAH-exciting far-UV photons from local energy sources (i.e., stars) are available there. Finally, in a normal starburst, stellar energy sources and gas/dust are spatially well mixed (Puxley 1991; McLeod et al. 1993; Forster Schreiber et al. 2001), so that the absolute optical depths of dust absorption features in the infrared spectra cannot exceed certain thresholds, whereas the optical depths can be arbitrarily large in a buried AGN, because the energy source (a compact mass-accreting SMBH) is more centrally concentrated than dust/gas (Imanishi & Maloney 2003; Imanishi et al. 2006, 2007). Thus, in principle, starbursts and buried AGNs are distinguishable on the basis of the strengths of PAH emission and dust absorption features in the infrared spectra.

From the low-resolution infrared 2.5–35 μm spectra of a large number of nearby ULIRGs, obtained with *ISO*, *Spitzer* and *AKARI* infrared satellites, the detectable buried AGN fraction has indeed been found to increase in ULIRGs, compared with galaxies with lower infrared luminosities (Tran et al. 2001; Imanishi et al. 2008; Imanishi 2009; Veilleux et al. 2009; Nardini et al. 2009). However, because the sample is not statistically complete, some bias and ambiguity could remain. Observations of a complete sample will clearly lead to a better understanding of the true nature of the nearby ULIRG population.

In this paper, we present the *Spitzer* IRS low-resolution infrared 5–35 μm spectra of previously unobserved, optically non-Seyfert ULIRGs at $z < 0.3$. By combining these data with our previous results (Imanishi et al. 2007; Imanishi 2009), we can carry out a systematic investigation of the energetic importance of buried AGNs in nearby ULIRGs, based on the complete sample. Throughout this paper, $H_0 = 75 \text{ km s}^{-1} \text{ Mpc}^{-1}$, $\Omega_M = 0.3$, and $\Omega_\Lambda = 0.7$ are adopted for the sake of consistency with our previously published papers.

2. TARGETS

The ULIRGs in the *IRAS* 1 Jy sample (Kim & Sanders 1998) are our targets. This sample consists of 118 ULIRGs at $z < 0.3$, whose *IRAS* 60 μm fluxes are larger than 1 Jy. Of these, 33 are optically classified as Seyferts, and 85 as non-Seyferts (Veilleux et al. 1999). The investigation of optically elusive, but intrinsically luminous, buried AGNs in the 85 optically non-Seyfert ULIRGs is our main objective. The 85 sources consist of 43 opti-

cally LINER, 32 optically HII-region, and 10 optically unclassified ULIRGs (Veilleux et al. 1999).

Imanishi et al. (2007) investigated the buried AGN fraction in the complete sample of 48 ULIRGs at $z < 0.15$, classified optically as LINERs and HII-regions, in the *IRAS* 1 Jy sample, on the basis of *Spitzer* low-resolution infrared 5–35 μm spectra. These authors found strong signatures of luminous buried AGNs in a sizable fraction (16/48; 33%) of the observed ULIRGs. Four optically unclassified ULIRGs at $z < 0.15$ were not studied.

Imanishi (2009) extended the *Spitzer* IRS low-resolution infrared spectroscopic study to ULIRGs at $z > 0.15$, classified optically as non-Seyferts (LINERs, HII-regions, and unclassified), in the *IRAS* 1 Jy sample, by analyzing the spectra of 20 sources available at that time. As a result of this extension, a large number of ULIRGs with $L_{\text{IR}} \geq 10^{12.3}L_\odot$ are now included, so that a meaningful investigation of the buried AGN fraction as a function of galaxy infrared luminosity has become possible, by dividing galaxies into different infrared luminosity classes. Specifically, the classes are defined by $L_{\text{IR}} < 10^{12}L_\odot$, $10^{12}L_\odot \leq L_{\text{IR}} < 10^{12.3}L_\odot$, and $L_{\text{IR}} \geq 10^{12.3}L_\odot$. Imanishi (2009) found a trend that the detectable buried AGN fraction systematically increases with increasing galaxy infrared luminosity. However, the ULIRG sample was not statistically complete, because unobserved, optically non-Seyfert ULIRGs remained in the *IRAS* 1 Jy sample.

Among 33 ULIRGs at $z > 0.15$ optically classified as non-Seyferts in the *IRAS* 1 Jy sample, five LINER, six HII-region, and two optically unclassified ULIRGs were not studied in Imanishi (2009). Additionally, four optically unclassified ULIRGs at $z < 0.15$ were not investigated by Imanishi et al. (2007) and Imanishi (2009). In total, there were 17 (20% of the total 85 sources) optically non-Seyfert ULIRGs without published *Spitzer* IRS 5–35 μm low-resolution spectra in the *IRAS* 1 Jy sample. Because *Spitzer* IRS 5–35 μm low-resolution spectroscopy of one source (*IRAS* 08474+1813) was scheduled in Cycle 3, we observed the remaining 16 ULIRGs on our own, during *Spitzer* Cycle 5. Table 1 summarizes the properties of these 17 ULIRGs.

3. OBSERVATIONS AND DATA ANALYSIS

Observations of all 17 ULIRGs were performed with the Infrared Spectrograph (IRS) (Houck et al. 2004) on board the *Spitzer* Space Telescope (Werner et al. 2004). All four modules, Short-Low 2 (SL2; 5.2–7.7 μm) and 1 (SL1; 7.4–14.5 μm), and Long-Low 2 (LL2; 14.0–21.3 μm) and 1 (LL1; 19.5–38.0 μm) were used to obtain the full 5–35 μm low-resolution ($R \sim 100$) spectra. Table 2 contains details of the observation log. The slit width was 3''6 or two pixels for SL2 (1''8 pixel $^{-1}$) and 3''7 or ~ 2 pixels for SL1 (1''8 pixel $^{-1}$). For LL2 and LL1, the slit widths were 10''5 and 10''7, respectively, corresponding to ~ 2 pixels for both LL2 (5''1 pixel $^{-1}$) and LL1 (5''1 pixel $^{-1}$).

The latest pipeline-processed data products available at the time of our analysis were used. Frames taken at position A were subtracted from those taken at position B to remove background emission, consisting mostly of zodiacal light. The spectra were then extracted in the standard manner. Apertures with 4–6 pixels were em-

ployed for SL and LL data. All sources were dominated by spatially compact emission whose size is similar to the PSF of SL and LL. The spectra extracted for the A and B positions were then summed. Wavelength and flux calibrations were made on the basis of the *Spitzer* pipeline-processed data. For the SL1 spectra, the data at $\lambda_{\text{obs}} > 14.5 \mu\text{m}$ in the observed frame are invalid (Infrared Spectrograph Data Handbook, version 1.0), and thus they were removed. For the LL1 spectra, the data at $\lambda_{\text{obs}} > 35 \mu\text{m}$ were not used, because they are noisy and not necessary for our scientific discussions.

For the flux calibration, we did not re-calibrate our spectra using the *IRAS* measurements at $12 \mu\text{m}$ and $25 \mu\text{m}$, because the *IRAS* $12 \mu\text{m}$ and/or $25 \mu\text{m}$ fluxes are only upper limits in many sources (Table 1). Hence, the absolute flux calibration is dependent on the accuracy of the pipeline-processed data, which is taken to be better than 20% for SL and LL (Infrared Spectrograph Data Handbook). This level of flux uncertainty does not significantly affect our main conclusions. For ULIRGs with *IRAS* $25 \mu\text{m}$ detection, we confirmed that the *Spitzer* IRS $25 \mu\text{m}$ flux agrees with the *IRAS* $25 \mu\text{m}$ data within 30%. For ULIRGs with *IRAS* $25 \mu\text{m}$ non-detection, the measured *Spitzer* IRS $25 \mu\text{m}$ flux is always smaller than the *IRAS* $25 \mu\text{m}$ upper limits.

For all ULIRGs, flux discrepancies between SL1 and LL2 were discernible, ranging from 40% to a factor of ~ 2 , and the SL1 flux ($3''7$ wide slit) was always smaller than the LL2 flux ($10''5$). The discrepancies were generally large in double-nuclei ULIRGs with separations of a few to several arcsec (marked sources in the column 1 of Table 2), possibly because the LL2 spectra cover the emission from both nuclei and a diffuse component, while the SL1 spectra only probe the emission from a brighter nucleus. We adjusted the SL1 (and SL2) flux to match the LL2 flux, to minimize missing PAH fluxes. Appropriate spectral binning with 2, 4, or 8 pixels was applied to reduce the scattering of data points particularly at SL2 ($5.2\text{--}7.7 \mu\text{m}$) and LL2 ($14.0\text{--}21.3 \mu\text{m}$) for faint ULIRGs, and at $\lambda_{\text{obs}} \sim 10 \mu\text{m}$ for ULIRGs that show deep $9.7 \mu\text{m}$ silicate dust absorption features.

4. RESULTS

The infrared $5\text{--}35 \mu\text{m}$ low-resolution spectra of the 17 observed ULIRGs are shown in Figure 1. The full $5\text{--}35 \mu\text{m}$ spectra of these ULIRGs are published here for the first time.

The spectra in Figure 1 are useful for observing the overall $5\text{--}35 \mu\text{m}$ spectral shapes and broad $9.7 \mu\text{m}$ and $18 \mu\text{m}$ silicate dust absorption features, but not for observing PAH emission. Following Imanishi et al. (2007) and Imanishi (2009), Figure 2 presents enlarged spectra at $\lambda_{\text{obs}} = 5.2\text{--}14.5 \mu\text{m}$ to better exhibit the PAH emission properties.

4.1. PAH emission

All ULIRGs in Figure 2 show clear signs of PAH emission at $\lambda_{\text{rest}} = 6.2 \mu\text{m}$, $7.7 \mu\text{m}$, and $11.3 \mu\text{m}$ in the rest frame. To estimate the strengths of these PAH emission, we adopted a linear continuum, following Imanishi et al. (2007) and Imanishi (2009). Data points at slightly shorter and longer wavelengths than the $6.2 \mu\text{m}$, $7.7 \mu\text{m}$, and $11.3 \mu\text{m}$ PAH emission were used to determine linear continuum levels, which are shown as solid lines in Figure

2. PAH emission features above the adopted continuum levels were fitted with Gaussian profiles. The estimated rest-frame equivalent widths (EW_{PAH}) and luminosities of the $6.2 \mu\text{m}$, $7.7 \mu\text{m}$, and $11.3 \mu\text{m}$ PAH emission are summarized in Table 3.

As noted by Imanishi et al. (2007) and Imanishi (2009), we estimated the strength of the $7.7 \mu\text{m}$ PAH emission in such a way that the uncertainty caused by the strong, broad $9.7 \mu\text{m}$ silicate dust absorption feature is minimized. This definition of the $7.7 \mu\text{m}$ PAH emission strength is significantly different from that used in previous papers (e.g., Genzel et al. 1998). We will not use $7.7 \mu\text{m}$ PAH emission strengths in our main discussions, because of the difficulty of comparing our data with data in the literature, as well as possible large uncertainties in the $7.7 \mu\text{m}$ PAH strengths.

4.2. Silicate absorption

To estimate the strengths of the silicate dust absorption features, we use $\tau'_{9.7}$ and τ'_{18} , defined by Imanishi et al. (2007). The value of $\tau'_{9.7}$ is the optical depth of the $9.7 \mu\text{m}$ silicate absorption feature, relative to a power-law continuum, determined from data points at $\lambda_{\text{rest}} = 7.1 \mu\text{m}$ and $14.2 \mu\text{m}$, to minimize the effects of PAH emission. The value of τ'_{18} is the optical depth of the $18 \mu\text{m}$ silicate absorption feature, relative to a power-law continuum determined from data points at $\lambda_{\text{rest}} = 14.2 \mu\text{m}$ and $24 \mu\text{m}$. These continua are shown as dotted lines in Figure 1. Because these continuum levels are determined using data points just outside the $9.7 \mu\text{m}$ and $18 \mu\text{m}$ features, and close to the absorption peaks, the measured optical depths are taken as true dips caused by the silicate dust absorption feature. The $\tau'_{9.7}$ and τ'_{18} values were estimated from several data points, close to the absorption peaks. The $\tau'_{9.7}$ values for all the ULIRGs are shown in Table 4 (column 2). The τ'_{18} values are also shown in Table 4 (column 3) for ULIRGs with clearly detected $18 \mu\text{m}$ silicate absorption features.

4.3. Ice absorption

Many ULIRGs display dips on the shorter wavelength side of the $6.2 \mu\text{m}$ PAH emission, which we ascribe to the $6.0 \mu\text{m}$ H_2O ice absorption feature (bending mode). Figure 3 presents enlarged spectra at $\lambda_{\text{obs}} = 5.2\text{--}9 \mu\text{m}$ for ULIRGs with clearly detected ice absorption features. The spectrum of IRAS 14202+2615 is also included, as an example of non-detection. The observed optical depths ($\tau_{6.0}$) are summarized in Table 5 for detected sources. The detection rate of this $6.0 \mu\text{m}$ ice absorption feature is substantially higher in optically LINER ULIRGs (5/5; 100%) than in HII-region ULIRGs (1/6; 17%).

5. DISCUSSION

For the sake of consistency, we use the criteria employed by Imanishi et al. (2007) and Imanishi (2009) to study buried AGNs in optically non-Seyfert ULIRGs. We first search for ULIRGs with luminous buried AGN signatures in infrared $5\text{--}35 \mu\text{m}$ spectra, and then estimate the extinction-corrected intrinsic luminosities of buried AGNs, based on the observed fluxes at $\sim 10 \mu\text{m}$ and dust extinction toward the $10 \mu\text{m}$ continuum emitting regions (Imanishi et al. 2007; Imanishi 2009).

Several other methods of evaluating the energetic importance of buried AGNs, based on *Spitzer* IRS infrared

low-resolution spectra, have been proposed in the literature (Veilleux et al. 2009; Nardini et al. 2009). In the methods of Veilleux et al. (2009), AGN and starburst zero-points were derived from *unobscured* AGNs and starburst galaxies, respectively. Then, relative buried AGN contributions to the *observed* fluxes of continuum and line emission at infrared 5–35 μm were derived. No dust extinction correction was applied to estimate buried AGN luminosities. Even though dust extinction at 5–35 μm is smaller than that at shorter wavelengths, using the *observed* fluxes could underestimate the intrinsic buried AGN luminosities, because emission from buried AGNs is more highly flux-attenuated than the surrounding starbursts in individual ULIRGs, as well as unobscured AGNs used to determine the AGN zero-points.

Nardini et al. (2009) applied dust extinction correction to estimate the intrinsic buried AGN luminosities, but their modeling utilized only 5–8 μm spectra. Our methods use a wider-wavelength range (5–35 μm) of *Spitzer* IRS spectra, and dust extinction is also taken into account to estimate the buried AGN luminosities.

5.1. Detected modestly obscured starbursts

Aside from the strong 9.7 μm silicate absorption peak, the flux attenuation of the continuum emission at $\lambda_{\text{rest}} > 5 \mu\text{m}$ is small (< 0.5 mag) for dust extinction with $A_V < 20$ mag (Nishiyama et al. 2008, 2009). Thus, the observed PAH emission luminosities at $\lambda_{\text{rest}} > 5 \mu\text{m}$ can be used to roughly estimate the intrinsic luminosities of modestly obscured ($A_V < 20$ mag) PAH-emitting normal starbursts (with PDRs and modest metallicity), provided that the PAH emission and infrared luminosities proportionally correlate in the starbursts (Peeters et al. 2004; Soifer et al. 2002). Since the metallicity of ULIRGs is estimated to be solar or even higher (Rupke et al. 2008; Veilleux et al. 2009), the assumption of PAH-emitting starbursts is valid in ULIRGs (Wu et al. 2006; Madden et al. 2006; O’Halloran et al. 2006; Smith et al. 2007). Table 3 (columns 8 and 9) lists the values of the 6.2 μm PAH to infrared luminosity ratio, $L_{6.2\text{PAH}}/L_{\text{IR}}$, and the 11.3 μm PAH to infrared luminosity ratio, $L_{11.3\text{PAH}}/L_{\text{IR}}$. In normal starburst galaxies with modest dust obscuration ($A_V < 20$ mag), the ratios are estimated to be $L_{6.2\text{PAH}}/L_{\text{IR}} \sim 3.4 \times 10^{-3}$ (Peeters et al. 2004) and $L_{11.3\text{PAH}}/L_{\text{IR}} \sim 1.4 \times 10^{-3}$ (Soifer et al. 2002)². Figure 4 compares the 6.2 μm and 11.3 μm PAH luminosities with the observed infrared luminosities.

The observed $L_{6.2\text{PAH}}/L_{\text{IR}}$ ratios are $(0.3\text{--}2.4) \times 10^{-3}$ (Table 3), or 9–71 % of 3.4×10^{-3} for modestly obscured starburst galaxies. In the majority of the observed ULIRGs, the ratios are $< 1.7 \times 10^{-3}$, or < 50 % of 3.4×10^{-3} (see also Figure 4). Taken at face value, the modestly obscured starbursts detected in these ULIRGs account for 9–71 % (mostly < 50 %) of their infrared luminosities. The same argument can be applied to the observed $L_{11.3\text{PAH}}/L_{\text{IR}}$ ratios for the ULIRGs. The $L_{11.3\text{PAH}}/L_{\text{IR}}$ ratios are $(0.3\text{--}1.8) \times 10^{-3}$ (Table 3), or 21–100 % of 1.4×10^{-3} for modestly obscured starburst galaxies. On the basis of the $L_{11.3\text{PAH}}/L_{\text{IR}}$ ratios, there

are some ULIRGs whose infrared luminosities can be explained by the detected modestly obscured ($A_V < 20$ mag) starbursts. However, for ULIRGs with $< 0.7 \times 10^{-3}$ (< 50 % of 1.4×10^{-3}), additional energy sources would be required. The 11.3 μm PAH emission tends to provide higher contributions from modestly obscured starbursts to the infrared luminosities of ULIRGs, than the 6.2 μm PAH emission (Figure 4), possibly because the 11.3 μm PAH emission originates in larger-sized PAHs which may be less susceptible to destruction by the energetic radiation from AGNs and intense starbursts in ULIRGs (Smith et al. 2007). Luminosities that are not accounted for by the detected modestly obscured starbursts might originate from (1) highly obscured ($A_V \gg 20$ mag) starbursts, in which the PAH emission flux is substantially attenuated by dust extinction, and/or (2) buried AGNs that produce strong infrared radiation, but virtually no PAH emission.

We note that emission from *extreme* starbursts, which consist of HII-regions only, without PDRs and molecular gas, can be PAH-free, because PAH molecules can be destroyed inside the HII-regions themselves (Sellgren 1981). If starbursts are exceptionally more centrally concentrated than the surrounding molecular gas and dust (Figure 1e of Imanishi et al. 2007), such HII-region-only starbursts could happen. However, in the case of ULIRG’s cores, such *extreme* starbursts require extremely high emission surface brightnesses, and so are unlikely (Imanishi et al. 2007), if not completely ruled out. We thus use the term “buried AGN signatures”, rather than “buried AGN evidence” throughout this manuscript.

5.2. ULIRGs that could contain luminous buried AGNs

5.2.1. Low equivalent width PAH emission

Highly-obscured normal starbursts and buried AGNs are basically distinguishable, based on the equivalent width of the PAH emission. A PAH equivalent width (EW_{PAH}) must always be large in a normal starburst (with PDRs) with a mixed dust/source geometry, regardless of the amount of dust extinction, because both the PAH and nearby continuum emission are similarly flux-attenuated. Thus, a small EW_{PAH} value suggests a contribution from a PAH-free continuum-emitting energy source, namely an AGN (Imanishi et al. 2007; Imanishi 2009).

Following Imanishi et al. (2007) and Imanishi (2009), we classify ULIRGs with $EW_{6.2\text{PAH}} < 180$ nm and $EW_{11.3\text{PAH}} < 200$ nm as sources displaying clear signatures of luminous AGNs, because a considerable contribution from a PAH-free continuum would be required for these sources. Figure 5 is a plot of the distribution of $EW_{6.2\text{PAH}}$ and $EW_{11.3\text{PAH}}$ values. Table 6 (columns 2–3) records the detection or non-detection of buried AGN signatures in terms of the PAH equivalent width threshold. The $EW_{6.2\text{PAH}}$ method provides a much larger buried AGN fraction (7/17; 41%) than the $EW_{11.3\text{PAH}}$ method (2/17; 12%), as seen in Imanishi et al. (2007) and Imanishi (2009). An explanation for this is that the 11.3 μm PAH emission feature is inside the strong 9.7 μm silicate dust absorption feature. Thus, the buried AGN continuum emission at $\lambda_{\text{rest}} \sim 11.3 \mu\text{m}$ is severely attenuated, and has little effect on the equivalent widths of the 11.3 μm PAH emission from less obscured starburst regions

² Smith et al. (2007) derived high PAH to infrared luminosity ratios, by including underlying plateau components as PAH fluxes. We employ the ratios obtained by Peeters et al. (2004) and Soifer et al. (2002), because of their similar continuum choices to ours.

outside the AGNs (Imanishi et al. 2007; Imanishi 2009).

5.2.2. Optical depths of dust absorption features

Based on the low EW_{PAH} method, a buried AGN with very weak starbursts is easily detectable. If strong starburst activity is present, AGN detection becomes difficult, but a *weakly obscured* AGN is still detectable, because dilution of the PAH emission by the AGN's PAH-free continuum can be significant. However, a *deeply buried* AGN with strong starbursts is very difficult to detect. Even if the intrinsic luminosity of a buried AGN is large, the AGN flux will be more highly attenuated by dust extinction than the surrounding starburst emission, keeping the observed EW_{PAH} value quite large.

To determine the presence of a deeply buried AGN with strong starbursts, we use the optical depths of the silicate dust absorption features. Specifically, these values can be used to distinguish whether the energy sources are spatially well mixed with dust (a normal starburst), or are more centrally concentrated than the dust (a buried AGN) (§1). Imanishi et al. (2007) obtained a maximum value of $\tau'_{9.7} = 1.7$ for a normal starburst with a mixed dust/source geometry. Considering the possible uncertainties of the $\tau'_{9.7}$ estimate, coming from continuum determination ambiguities and statistical errors of individual data points, we classify ULIRGs with $\tau'_{9.7} \geq 2$ as potential locations of luminous, but deeply buried AGNs with centrally concentrated energy source geometries. Five ULIRGs have $\tau'_{9.7} \geq 2$ (Tables 4 and 6).

As noted by Imanishi (2009), although this large $\tau_{9.7}$ method is sensitive to deeply buried AGNs, it is obviously insensitive to weakly obscured AGNs, which are better probed with the low EW_{PAH} method. Thus, the low EW_{PAH} and large $\tau_{9.7}$ methods are complementary to each other. At the same time, a normal starburst nucleus with a mixed dust/source geometry and a large amount of *foreground screen dust in an edge-on host galaxy* (Figure 1d of Imanishi et al. 2007), and an exceptionally centrally-concentrated starburst (Figure 1e of Imanishi et al. 2007), are capable of producing large $\tau'_{9.7}$ values. However, it is unlikely that the majority of the ULIRGs with $\tau'_{9.7} \geq 2$ fit these non-AGN cases (Imanishi et al. 2007; Imanishi 2009).

5.2.3. Strong dust temperature gradients

As explained by Imanishi et al. (2007), a buried AGN with a centrally concentrated energy source geometry should have a strong dust temperature gradient, because the inner dust (close to the central energy source) has a higher temperature than the outer dust, whereas a normal starburst nucleus with a mixed dust/source geometry does not exhibit this behavior. The presence of a strong dust temperature gradient could be detected by comparing the optical depths of the 9.7 μm and 18 μm silicate dust absorption features, as long as the contaminations from weakly obscured starbursts to observed infrared fluxes are not severe. $\tau'_{18}/\tau'_{9.7} < 0.3$ could be taken as the signature of a strong dust temperature gradient (Imanishi et al. 2007; Imanishi 2009). This could provide an additional signature for a buried AGN. Although this was the case for 12 sources studied by Imanishi et al. (2007) and Imanishi (2009), no such case was found among the 17 newly observed ULIRGs (Table 4, column

4). Because of the contamination from weakly obscured starburst activity, as well as other possible ambiguities (Imanishi et al. 2007), not all buried AGNs actually satisfy $\tau'_{18}/\tau'_{9.7} < 0.3$. The criterion $\tau'_{18}/\tau'_{9.7} < 0.3$ is a sufficient condition for an additional signature of a buried AGN, but it is not a necessary condition.

5.2.4. Combination of energy diagnostic methods

Table 6 (column 5) summarizes the strengths of the detected buried AGN signatures in the *Spitzer* IRS 5–35 μm spectra, based on the (1) low EW_{PAH} and (2) large $\tau'_{9.7}$ methods. If buried AGN signatures are found by both methods, or by the first method, the ULIRGs are classified as *strong* buried AGN candidates, marked with open circles. Eight ULIRGs show strong signatures of luminous buried AGNs (Table 6).

The detection rate of luminous buried AGNs in the newly observed optically non-Seyfert ULIRGs (8/17; 47%) is significantly smaller than the rate obtained by Imanishi (2009) (14/20; 70%). This may be partly due to the smaller fraction of ULIRGs with $L_{\text{IR}} \geq 10^{12.3} L_{\odot}$ (6/17; 35%) in this sample, compared with Imanishi (2009) (17/20; 85%).

5.2.5. Extinction-corrected intrinsic buried AGN luminosities

For ULIRGs with very low PAH equivalent widths, the observed fluxes are taken to be mostly the result of AGN-heated, PAH-free dust continuum emission. We can estimate the extinction-corrected intrinsic dust emission luminosity at $\sim 10 \mu\text{m}$ (νF_{ν}), heated by the AGN, on the basis of the observed fluxes at $\lambda_{\text{rest}} \sim 10 \mu\text{m}$ and dust extinction toward the 10 μm continuum emitting regions inferred from $\tau'_{9.7}$ (Imanishi et al. 2007; Imanishi 2009). As argued by Imanishi et al. (2007) and Imanishi (2009), in a pure AGN with a simple spherical dust distribution, dust emission luminosity is conserved at each temperature from hot inside regions to cool outside regions (Figure 2 of Imanishi et al. 2007). The extinction-corrected 10 μm luminosity (νF_{ν}) should be comparable to the intrinsic luminosity of the AGN's primary radiation.

To obtain the estimate, we followed Imanishi et al. (2007) and Imanishi (2009). The flux attenuation of the 8 or 13 μm continuum outside the 9.7 μm silicate feature is $10^{\tau'_{9.7}/2.3/2.5}$ (Rieke & Lebofsky 1985), and ranges from a factor of 1.3 (IRAS 14202+2615; $\tau'_{9.7} \sim 0.7$) to 3.3 (IRAS 04074–2801; $\tau'_{9.7} \sim 3.0$). We found that the extinction-corrected intrinsic buried AGN luminosities for selected ULIRGs with very low EW_{PAH} values are a few $\times 10^{45}$ ergs s^{-1} , or $\sim 10^{12} L_{\odot}$ in the maximum case (Table 7). Figure 6 compares the intrinsic buried AGN luminosity and the infrared luminosity. The detected buried AGNs could explain a significant, but not dominant fraction (6–33%), of the luminosities of these ULIRGs. In Table 7, the luminosities of the detected modestly obscured starbursts, estimated from the $L_{6.2\text{PAH}}$ and $L_{11.3\text{PAH}}$ values, are also listed for the sake of comparison.

Our method to estimate the intrinsic buried AGN luminosities is very simple and straightforward, with a small amount of free parameters. The largest possible uncertainty is dust extinction curve in ULIRGs, which might be different from that established in the Galactic interstellar medium which we adopted. Different dust grain

size distribution can produce different dust extinction ratio between widely separate wavelengths, such as optical and 10 μm . However, as mentioned by Imanishi et al. (2007; their Appendix), our estimate is dependent only on the dust extinction ratio between 8 or 13 μm continuum and $\tau'_{9.7}$, which should be insensitive to dust size distribution, because of the proximity of the wavelengths. Hence, our method is robust to this possible uncertainty.

5.3. Buried AGN fraction as a function of galaxy infrared luminosity

Imanishi et al. (2007) investigated the presence of luminous buried AGNs in 48 ULIRGs at $z < 0.15$, classified optically as non-Seyferts (28 LINER and 20 HII-region ULIRGs). Imanishi (2009) did the same in 20 ULIRGs at $z > 0.15$, classified optically as non-Seyferts (10 LINER, 6 HII-region, 4 unclassified ULIRGs). In the present research, we have continued this work in 13 optically non-Seyfert ULIRGs at $z > 0.15$ (5 LINER, 6 HII-region, 2 unclassified ULIRGs) and four optically unclassified ULIRGs at $z < 0.15$. Taken together, these 85 observed sources comprise a *complete* sample of optically non-Seyfert ULIRGs in the *IRAS* 1 Jy sample.

Following Imanishi (2009), we divide the observed ULIRGs into those with $10^{12}\text{L}_{\odot} \leq L_{\text{IR}} < 10^{12.3}\text{L}_{\odot}$ and those with $L_{\text{IR}} \geq 10^{12.3}\text{L}_{\odot}$. After combining the results of Imanishi et al. (2007), Imanishi (2009) and this paper, we summarize the detectable buried AGN fraction in Table 8. Using this complete sample, we confirm the previously discovered trend (Imanishi et al. 2008; Imanishi 2009; Veilleux et al. 2009; Nardini et al. 2009) that the detectable buried AGN fraction is significantly higher in ULIRGs with $L_{\text{IR}} \geq 10^{12.3}\text{L}_{\odot}$ (22/31; 71%) than in those with $10^{12}\text{L}_{\odot} \leq L_{\text{IR}} < 10^{12.3}\text{L}_{\odot}$ (15/54; 28%). Figure 7 illustrates this trend by including galaxies with $L_{\text{IR}} < 10^{12}\text{L}_{\odot}$. Figure 5 displays the distributions of $\text{EW}_{6.2\text{PAH}}$, $\text{EW}_{11.3\text{PAH}}$ and $\tau'_{9.7}$ as functions of galaxy infrared luminosity. It is clear that the fraction of galaxies that meet the requirements for a buried AGN increases with increasing galaxy infrared luminosity in all plots.

In Table 8, we also find that buried AGNs are more important in LINER ULIRGs (21/43; 49%) than in HII-region ULIRGs (12/32; 38%), as has been previously suggested (Imanishi et al. 2006, 2007, 2008; Imanishi 2009). However, the difference is now small in this complete sample, and is possibly caused by a higher fraction of ULIRGs with $L_{\text{IR}} \geq 10^{12.3}\text{L}_{\odot}$ in the LINER sample (18/43; 42%) than in the HII-region sample (10/32; 31%) (Table 8). The buried AGN fraction is also higher in ULIRGs at $z > 0.15$ than in those at $z \leq 0.15$, but this may be due to the presence of a larger fraction of more luminous ULIRGs in a more distant sample.

For an AGN surrounded by dust with a torus-shaped distribution, the visibility of the central AGN is expected to increase with increasing AGN luminosity, because the innermost dust sublimation radius of the torus is proportional to the square root of the central AGN luminosity, and thus (assuming a constant torus scale height) the opening angle of the AGN is greater in luminous AGNs (the so-called receding torus model: Lawrence 1991; Simpson 2005; Arshakian 2005). In this scenario, the fraction of optically elusive buried AGNs is not large in luminous AGNs. However, this model is applicable *only if* the total amount of dust surrounding the central

AGN does not vary significantly, depending on the galaxy and AGN luminosity. ULIRGs are driven by mergers of gas-rich galaxies, and gas/dust is quickly transported to the nuclear regions by the gravitational torques, producing a highly-concentrated nuclear gas/dust distribution (Hopkins et al. 2006). AGNs can be easily buried by the increasing amount of nuclear gas/dust surrounding the central AGNs, and thus we believe that a high buried AGN fraction is a natural state of affairs in ULIRGs.

The higher fractions of buried AGNs (found in this work) and optical Seyferts (Veilleux et al. 1999; Goto 2005) indicate that AGNs become intrinsically more important with increasing galaxy infrared luminosity. Namely, *the AGN-starburst connections depend on galaxy luminosity*. This is the primary consequence of our results.

Figure 6 suggests that AGN's energetic contributions are generally 10–50%, or $\sim 30\%$ in median value, in ULIRGs with buried AGN signatures, which roughly agrees with other independent estimates (Veilleux et al. 2009; Nardini et al. 2009) in overall ULIRG sample. If 30% of the infrared luminosity comes from a buried AGN in a ULIRG with $L_{\text{IR}} = 10^{12.3}\text{L}_{\odot}$ ($= 2 \times 10^{12}\text{L}_{\odot}$), then the remaining infrared luminosity, originating in starbursts (including highly obscured $A_V \gg 20$ mag ones), is $1.4 \times 10^{12}\text{L}_{\odot}$. In the meanwhile, buried AGN contribution is generally insignificant in galaxies with $L_{\text{IR}} = 10^{11.3}\text{L}_{\odot}$ ($= 2 \times 10^{11}\text{L}_{\odot}$) (Figure 7), and in this case, the starburst-originating luminosity is $\sim 2 \times 10^{11}\text{L}_{\odot}$. Namely, in ULIRGs, the *relative* energetic importance of buried AGN is higher, but the *absolute* luminosities of starbursts, and thereby the star-formation rates, are also higher than galaxies with lower infrared luminosities. Unless the starburst duration time is drastically different, ULIRGs will produce more stars in the future, and evolve into more massive galaxies with larger stellar masses, than less infrared luminous galaxies.

Given the mass correlation between SMBH and spheroidal stellar component (Magorrian et al. 1998; Ferrarese & Merritt 2000), galaxies with lower infrared luminosities should also contain SMBHs whose masses are proportional to those of spheroidal stars. The higher AGN contributions in ULIRGs suggest that SMBHs in ULIRGs (progenitors of massive galaxies) are actively mass-accreting, and consequently, can have stronger radiation feedbacks to the surrounding gas and dust than mildly mass accreting SMBHs in less infrared luminous galaxies. A related phenomenon may be galaxy downsizing, where the more massive galaxies (with currently larger stellar masses) completed their major star formation during an earlier cosmic age (Cowie et al. 1996; Bundy et al. 2005). It has been suggested that in these more massive galaxies, AGN feedback was stronger in the past, heating or expelling gas and suppressing further star formation over a shorter time scale (Granato et al. 2004; Bower et al. 2006; Sijacki et al. 2007). Buried AGNs surrounded by a large amount of gas and dust may have particularly strong feedback, compared to already visible AGNs with a relatively thin dust covering, and thus are the important population for determining the interplay between AGNs and host galaxies.

Figure 8 illustrates our findings that *buried AGNs are relatively more important energetically in galaxies that are currently more infrared luminous, and in the future,*

these galaxies will evolve into more massive galaxies with larger stellar masses. The energetic contributions from buried AGNs become discernible in ULIRGs, which are thought to evolve into galaxies with stellar masses of several $\times 10^{10}M_{\odot}$, based on infrared velocity dispersion measurements of ULIRG's host galaxies (Dasyra et al. 2006). A similar eventual spheroidal stellar mass is derived for ULIRGs with detectable buried AGN signatures, from the intrinsic buried AGN luminosities (Imanishi 2009), if we assume that AGN luminosities are Eddington limits and if the widely accepted mass correlation between SMBHs and spheroidal stellar components holds (Magorrian et al. 1998; Ferrarese & Merritt 2000). This mass with several $\times 10^{10}M_{\odot}$ roughly corresponds to the stellar mass that separates red, massive galaxies with low current star formation rates (major star formation has already been completed) and blue, less massive galaxies with ongoing active star formation in the local universe (Kauffmann et al. 2003). Thus, our results may offer support to the AGN feedback scenario as the origin of the galaxy downsizing phenomenon.

6. SUMMARY

We have presented the results of *Spitzer* IRS infrared 5–35 μm low-resolution ($R \sim 100$) spectroscopy of 17 nearby ULIRGs at $z < 0.2$, optically classified as non-Seyferts (LINERs, HII-regions, and unclassified, i.e., no optical AGN signatures). Optically elusive, but intrinsically luminous buried AGNs were searched for in these optically non-Seyfert ULIRGs, on the basis of the strengths of PAH emission and silicate dust absorption features. We then combined these results with those of our previous studies of nearby ULIRGs, using *Spitzer* IRS, to investigate the energetic importance of buried AGNs in a *complete sample* of optically non-Seyfert ULIRGs in the local universe at $z < 0.3$ (85 sources altogether). We arrived at the following primary conclusions.

1. Among the 17 newly observed optically non-Seyfert ULIRGs, the signatures of important energy contributions from buried AGNs were found in eight sources. In these sources, the extinction-corrected intrinsic buried AGN luminosities were estimated at up to $\sim 10^{12}L_{\odot}$, accounting for a significant fraction (6–33%) of the observed infrared luminosities of these ULIRGs.
2. By combining our new results with those of our previous studies (Imanishi et al. 2007; Imanishi 2009), we found that buried AGNs are energetically

important in 37 sources of the complete ULIRG sample of 85 ($37/85 = 44\%$), confirming previous suggestion that optically elusive, luminous buried AGNs are common in the ULIRGs of the local universe.

3. We investigated the fraction of detectable luminous buried AGNs by separating ULIRGs with $10^{12}L_{\odot} \leq L_{\text{IR}} < 10^{12.3}L_{\odot}$ (54 sources) and $L_{\text{IR}} \geq 10^{12.3}L_{\odot}$ (31 sources). We found that luminous buried AGNs were much more common in the latter ULIRGs ($22/31 = 71\%$) than in the former ULIRGs ($15/54 = 28\%$), confirming the previous arguments that buried AGNs become more energetically important with increasing galaxy infrared luminosity.
4. Given the higher fraction of optical Seyferts (optically identified AGNs) in ULIRGs with higher infrared luminosities, luminous AGNs are more common in ULIRGs with $L_{\text{IR}} \geq 10^{12.3}L_{\odot}$ than in ULIRGs with $10^{12}L_{\odot} \leq L_{\text{IR}} < 10^{12.3}L_{\odot}$. Because the detection rate of both optically identified Seyfert AGNs and optically elusive buried AGNs is substantially lower in galaxies with lower infrared luminosities ($L_{\text{IR}} < 10^{12}L_{\odot}$), we can conclude that the energetic importance of AGNs increases with increasing galaxy infrared luminosity, suggesting that *the AGN-starburst connections are luminosity dependent*. This may be related to the widely-proposed AGN feedback scenario for the galaxy downsizing phenomenon.

This work is based on observations made with the *Spitzer* Space Telescope, operated by the Jet Propulsion Laboratory at California Institute of Technology, under a contract with NASA. Support for this work was provided by NASA, and also by an award issued by JPL/Caltech. We thank the anonymous referee for his/her valuable comments which help significantly improve the clarity of the arguments in this manuscript. M.I. is supported by Grants-in-Aid for Scientific Research (19740109). R.M. acknowledges partial support from INAF and ASI, through contract ASI-INAF I/016/07/0. This research made use of the SIMBAD database, operated at CDS, Strasbourg, France, and the NASA/IPAC Extragalactic Database (NED), which is operated by the Jet Propulsion Laboratory at California Institute of Technology, under a contract with NASA.

REFERENCES

- Arshakian, T. G. 2005, *A&A*, 436, 817
 Armus, L., et al. 2007, *ApJ*, 656, 148
 Bower, R. G., Benson, A. J., Malbon, R., Helly, J. C., Frenk, C. S., Baugh, C. M., Cole, S., & Lacey, C. G. 2006, *MNRAS*, 370, 645
 Brandl, B. R., et al. 2006, *ApJ*, 653, 1129
 Bundy, K., Ellis, R. S., & Conselice, C. J. 2005, *ApJ*, 625, 621
 Caputi, K. I., et al. 2007, *ApJ*, 660, 97
 Cowie, L. L., Songaila, A., Hu, E. M., & Cohen, J. G. 1996, *AJ*, 112, 839
 Dasyra, K. M., et al. 2006, *ApJ*, 651, 835
 Desai, V., et al. 2007, *ApJ*, 669, 810
 Farrah, D., et al. 2007, *ApJ*, 667, 149
 Ferrarese, L., & Merritt, D. 2000, *apJ*, 539, L9
 Forster Schreiber, N. M., Genzel, R., Lutz, D., Kunze, D., & Sternberg, A. 2001, *ApJ*, 552, 544
 Genzel, R. et al. 1998, *ApJ*, 498, 579
 Goto, T. 2005, *MNRAS*, 360, 322
 Granato, G. L., De Zotti, G., Silva, L., Bressan, A., & Danese, L. 2004, *ApJ*, 600, 580
 Hopkins, P. F., Hernquist, L., Cox, T. J., Di Matteo, T., Martini, P., Robertson, B., & Springel, V. 2005, *ApJ*, 630, 705
 Hopkins, P. F., Hernquist, L., Cox, T. J., Di Matteo, T., Robertson, B., & Springel, V. 2006, *ApJS*, 163, 1
 Houck, J. R., et al. 2004, *ApJS*, 154, 18
 Imanishi, M. 2009, *ApJ*, 694, 751
 Imanishi, M., & Dudley, C. C. 2000, *ApJ*, 545, 701
 Imanishi, M., & Maloney, P. R. 2003, *ApJ*, 588, 165

- Imanishi, M., Dudley, C. C., & Maloney, P. R. 2006, *ApJ*, 637, 114
Imanishi, M., Dudley, C. C., Maiolino, R., Maloney, P. R., Nakagawa, T., & Risaliti, G. 2007, *ApJS*, 171, 72
Imanishi, M., Nakagawa, T., Ohyama, Y., Shirahata, M., Wada, T., Onaka, T., & Oi, N. 2008, *PASJ*, S489
Kauffmann, G., et al. 2003, *MNRAS*, 341, 54
Kewley, L. J., Groves, B., Kauffmann, G., & Heckman, T. 2006, *MNRAS*, 372, 961
Kim, D. -C., & Sanders, D. B., 1998, *ApJS*, 119, 41
Kim, D. -C., Veilleux, S., & Sanders, D. B., 2002, *ApJS*, 143, 277
Lawrence A. 1991, *MNRAS*, 252, 586
Madden, S. C., Galliano, F., Jones, A. P., & Sauvage, M., 2006, *A&A*, 446, 877
Magorrian, J., et al. 1998, *ApJ*, 115, 2285
Maiolino, R. et al. 2003, *MNRAS*, 344, L59
McLeod, K. K., Rieke, G. H., Rieke, M. J., & Kelly, D. M. 1993, *ApJ*, 412, 111
Moorwood, A. F. M. 1986, *A&A*, 166, 4
Nardini, E., Risaliti, G., Salvati, M., Sani, E., Watabe, Y., Marconi, A., & Maiolino, R. 2009, *MNRAS*, 399, 1373
Nishiyama, S., Nagata, T., Tamura, M., Kandori, R., Hatano, H., Sato, S., & Sugitani, K. 2008, *ApJ*, 680, 1174
Nishiyama, S., Tamura, M., Hatano, H., Kato, D., Tanabe, T., Sugitani, K., & Nagata, T. 2009, *ApJ*, 696, 1407
O'Halloran, B., Satyapal, S., & Dudik, R. P., 2006, *ApJ*, 641, 795
Peeters, E., Spoon, H. W. W., & Tielens, A. G. G. M. 2004, *ApJ*, 613, 986
Rieke, G. H., & Lebofsky, M. J. 1985, *ApJ*, 288, 618
Puxley, P. J. 1991, *MNRAS*, 249, 11p
Roche, P. F., Aitken, D. K., Smith, C. H., & Ward, M. J., 1991, *MNRAS*, 248, 606
Rupke, D. S. N., Veilleux, S., & Baker, A. J. 2008, *ApJ*, 674, 172
Sanders, D. B., & Mirabel, I. F. 1996, *ARA&A*, 34, 749
Sanders, D. B., Soifer, B. T., Elias, J. H., Madore, B. F., Matthews, K., Neugebauer, G., & Scoville, N. Z. 1988a, *ApJ*, 325, 74
Sanders, D. B., Soifer, B. T., Elias, J. H., Neugebauer, G., & Matthews, K. 1988b, *ApJ*, 328, L35
Sellgren, K. 1981, *ApJ*, 245, 138
Sijacki, D., Springel, V., Di Matteo, T., & Hernquist, L. 2007, *MNRAS*, 380, 877
Simpson, C. 2005, *MNRAS*, 360, 565
Smith, J. D., et al. 2007, *ApJ*, 656, 770
Soifer, B. T. et al. 2000, *AJ*, 119, 509
Soifer, B. T. et al. 2001, *AJ*, 122, 1213
Soifer, B. T., Neugebauer, G., Matthews, K., Egami, E., & Weinberger, A. J. 2002, *AJ*, 124, 2980
Tran, Q. D., et al. 2001, *ApJ*, 552, 527
Veilleux, S., Kim, D. -C., & Sanders, D. B. 1999, *ApJ*, 522, 113
Veilleux, S., & Osterbrock, D. E. 1987, *ApJS*, 63, 295
Veilleux, S., et al. 2009, *ApJS*, 182, 628
Voit, G. M. 1992, *MNRAS*, 258, 841
Werner, M. W., et al. 2004, *ApJS*, 154, 1
Wu, Y., Charmandaris, V., Hao, L., Brandl, B. R., Bernard-Salas, J., Spoon, H. W. W., & Houck, J. R. 2006, *ApJ*, 639, 157

TABLE 1
OBSERVED ULIRGS AND THEIR *IRAS*-BASED INFRARED EMISSION PROPERTIES

Object	Redshift	f_{12} (Jy)	f_{25} (Jy)	f_{60} (Jy)	f_{100} (Jy)	$\log L_{\text{IR}}$ L_{\odot}	f_{25}/f_{60}	Optical Class
(1)	(2)	(3)	(4)	(5)	(6)	(7)	(8)	(9)
IRAS 04074–2801	0.153	<0.07	0.07	1.33	1.72	12.2	0.05 (C)	LINER
IRAS 05020–2941	0.154	<0.06	0.10	1.93	2.06	12.3	0.05 (C)	LINER
IRAS 13106–0922	0.174	<0.12	<0.06	1.24	1.89	12.3	<0.05 (C)	LINER
IRAS 14121–0126	0.151	0.06	0.11	1.39	2.07	12.3	0.08 (C)	LINER
IRAS 21477+0502	0.171	<0.09	0.16	1.14	1.46	12.3	0.14 (C)	LINER
IRAS 03209–0806	0.166	<0.10	<0.13	1.00	1.69	12.2	<0.13 (C)	HII-region
IRAS 10594+3818	0.158	<0.09	<0.15	1.29	1.89	12.2	<0.12 (C)	HII-region
IRAS 12447+3721	0.158	<0.12	0.10	1.04	0.84	12.1	0.10 (C)	HII-region
IRAS 14202+2615	0.159	0.18	0.15	1.49	1.99	12.4	0.10 (C)	HII-region
IRAS 15043+5754	0.151	<0.12	0.07	1.02	1.50	12.1	0.07 (C)	HII-region
IRAS 22088–1831	0.170	<0.09	0.07	1.73	1.73	12.4	0.04 (C)	HII-region
IRAS 02480–3745	0.165	<0.05	<0.11	1.25	1.49	12.2	<0.09 (C)	unclassified
IRAS 08591+5248	0.158	<0.10	<0.16	1.01	1.53	12.2	<0.16 (C)	unclassified
IRAS 02021–2103	0.116	<0.07	0.30	1.45	1.72	12.0	0.21 (W)	unclassified
IRAS 08474+1813	0.145	<0.10	<0.19	1.28	1.54	12.1	<0.15 (C)	unclassified
IRAS 14197+0813	0.131	<0.17	<0.19	1.10	1.66	12.0	<0.18 (C)	unclassified
IRAS 14485–2434	0.148	<0.11	<0.15	1.02	1.05	12.1	<0.15 (C)	unclassified

NOTE. — Col.(1): Object name. Col.(2): Redshift. Col.(3)–(6): f_{12} , f_{25} , f_{60} , and f_{100} are *IRAS* fluxes at 12 μm , 25 μm , 60 μm , and 100 μm in [Jy], respectively, taken from Kim & Sanders (1998). Col.(7): Decimal logarithm of infrared (8–1000 μm) luminosity in units of solar luminosity (L_{\odot}), calculated with $L_{\text{IR}} = 2.1 \times 10^{39} \times D(\text{Mpc})^2 \times (13.48 \times f_{12} + 5.16 \times f_{25} + 2.58 \times f_{60} + f_{100}) \text{ ergs s}^{-1}$ (Sanders & Mirabel 1996). Because the calculation is based on our adopted cosmology, the infrared luminosities differ slightly (<10%) from the values shown in Kim & Sanders (1998, Table 1, column 15). For sources with upper limits in some *IRAS* band, we can derive the respective upper and lower limits for infrared luminosity, assuming that the actual flux is between the *IRAS*-upper limit and zero. The difference in the upper and lower values is usually very small, less than 0.25 dex. We assume that the infrared luminosity is the average of these values. Col.(8): *IRAS* 25 μm to 60 μm flux ratio. ULIRGs with $f_{25}/f_{60} < 0.2$ and > 0.2 are classified as cool and warm sources (denoted as “C” and “W”), respectively (Sanders et al. 1988b). Col.(9): Optical spectral classification by Veilleux et al. (1999).

TABLE 2
Spitzer IRS OBSERVING LOG

Object	PID	Date [UT]	Integration time [sec]			
			SL2	SL1	LL2	LL1
(1)	(2)	(3)	(4)	(5)	(6)	(7)
IRAS 04074–2801	50008	2009 Mar 8	480	480	240	240
IRAS 05020–2941	50008	2008 Dec 5	240	240	240	240
IRAS 13106–0922	50008	2009 Mar 6	480	480	240	240
IRAS 14121–0126	50008	2009 Mar 5	240	240	240	240
IRAS 21477+0502 ^a	50008	2008 Dec 5	960	960	480	480
IRAS 03209–0806	50008	2009 Mar 8	480	480	240	240
IRAS 10594+3818 ^b	50008	2009 Jan 11, 15	960	960	480	480
IRAS 12447+3721	50008	2009 Jan 24	240	240	240	240
IRAS 14202+2615 ^c	50008	2009 Mar 3, 2009 Apr 2	480	480	480	480
IRAS 15043+5754 ^d	50008	2009 Feb 26	960	960	480	480
IRAS 22088–1831 ^e	50008	2008 Dec 5	960	960	480	480
IRAS 02480–3745	50008	2009 Jan 25	240	240	240	240
IRAS 08591+5248	50008	2008 Dec 9	240	240	240	240
IRAS 02021–2103	3187 + 50008	2005 Jan 15, 2009 Jan 15	240	240	240	240
IRAS 08474+1813	30407	2007 Dec 5	168	168	180	180
IRAS 14197+0813	3187 + 50008	2005 Feb 13, 2009 Mar 3	240	240	240	240
IRAS 14485–2434	50008	2009 Apr 6	240	240	240	240

NOTE. — Col.(1): Object name. Col.(2): PID number: 50008 (PI: Imanishi), 3187 (PI: Veilleux), and 30407 (PI: Darling). Col.(3): Observing date in UT. Col.(4): Net on-source integration time for SL2 spectroscopy in [sec]. Col.(5): Net on-source integration time for SL1 spectroscopy in [sec]. Col.(6): Net on-source integration time for LL2 spectroscopy in [sec]. Col.(7): Net on-source integration time for LL1 spectroscopy in [sec].

^aAlthough separate spectroscopy of E and W nuclei with a separation of ~ 7.5 arcsec (Kim et al. 2002) had been proposed, the E nucleus was observed.

^bAlthough separate spectroscopy of SW and NE nuclei with a separation of ~ 2 arcsec (Kim et al. 2002) had been proposed, the SW nucleus was observed.

^cAlthough separate spectroscopy of SE and NW nuclei with a separation of ~ 6 arcsec (Kim et al. 2002) had been proposed, the SE nucleus was observed.

^dAlthough separate spectroscopy of S and N nuclei with a separation of ~ 2.5 arcsec (Kim et al. 2002) had been proposed, the S nucleus was observed.

^eAlthough separate spectroscopy of E and W nuclei with a separation of ~ 2 arcsec (Kim et al. 2002) had been proposed, the E-nucleus was observed.

TABLE 3
OBSERVED PROPERTIES OF PAH EMISSION FEATURES

Object	EW _{6.2PAH} [nm]	EW _{7.7PAH} ^a [nm]	EW _{11.3PAH} [nm]	L _{6.2PAH} 10 ⁴² [ergs s ⁻¹]	L _{7.7PAH} ^a 10 ⁴² [ergs s ⁻¹]	L _{11.3PAH} 10 ⁴² [ergs s ⁻¹]	L _{6.2PAH} /L _{IIR} [× 10 ⁻³]	L _{11.3PAH} /L _{IIR} [× 10 ⁻³]
(1)	(2)	(3)	(4)	(5)	(6)	(7)	(8)	(9)
IRAS 04074–2801	60	420	235	3.3	32.8	2.5	0.6	0.4
IRAS 05020–2941	130	605	330	7.0	47.1	4.2	0.9	0.5
IRAS 13106–0922	115	425	565	3.3	27.6	3.5	0.4	0.4
IRAS 14121–0126	270	635	345	11.9	38.2	7.8	1.7	1.2
IRAS 21477+0502	235	575	185	7.4	24.2	5.4	1.0	0.7
IRAS 03209–0806	285	555	410	9.9	26.4	9.2	1.6	1.5
IRAS 10594+3818	350	780	490	16.0	46.0	11.1	2.4	1.7
IRAS 12447+3721	210	625	260	7.0	24.0	4.1	1.4	0.8
IRAS 14202+2615	160	455	265	18.7	52.9	13.6	1.9	1.4
IRAS 15043+5754	285	770	555	8.0	29.3	6.7	1.6	1.3
IRAS 22088–1831	90	455	195	3.0	23.6	2.3	0.3	0.3
IRAS 02480–3745	325	915	535	7.3	25.6	5.0	1.2	0.8
IRAS 08591+5248	310	695	535	9.7	30.7	9.7	1.8	1.8
IRAS 02021–2103	285	490	275	5.5	13.0	4.2	1.4	1.0
IRAS 08474+1813	170	985	285	2.2	13.1	1.4	0.4	0.3
IRAS 14197+0813	305	565	325	3.8	11.4	3.7	0.9	0.9
IRAS 14485–2434	150	495	295	6.8	26.2	6.8	1.6	1.6

NOTE. — Col.(1): Object name. Col.(2): Rest-frame equivalent width of the 6.2 μm PAH emission in [nm]. Col.(3): Rest-frame equivalent width of the 7.7 μm PAH emission in [nm]. Col.(4): Rest-frame equivalent width of the 11.3 μm PAH emission in [nm]. Col.(5): Luminosity of the 6.2 μm PAH emission in units of 10^{42} [ergs s⁻¹]. Col.(6): Luminosity of the 7.7 μm PAH emission in units of 10^{42} [ergs s⁻¹]. Col.(7): Luminosity of the 11.3 μm PAH emission in units of 10^{42} [ergs s⁻¹]. Col.(8): The 6.2 μm PAH to infrared luminosity ratio in units of 10^{-3} . The ratio for normal starbursts with modest dust obscuration ($A_V < 20$ mag) is $\sim 3.4 \times 10^{-3}$ (Peeters et al. 2004). Col.(9): The 11.3 μm PAH to infrared luminosity ratio in units of 10^{-3} . The ratio for normal starbursts with modest dust obscuration ($A_V < 20$ mag) is $\sim 1.4 \times 10^{-3}$ (Soifer et al. 2002).

^aWe consider the flux excess at $\lambda_{\text{rest}} = 7.3\text{--}8.1$ μm above an adopted continuum level to be 7.7 μm PAH emission, to reduce the effects of the strong 9.7 μm silicate dust absorption feature. The 7.7 μm PAH emission strengths may be significantly different from those estimated by other authors.

TABLE 4
OPTICAL DEPTH OF THE 9.7 μM AND 18 μM
SILICATE DUST ABSORPTION FEATURE

Object (1)	$\tau'_{9.7}$ (2)	τ'_{18} (3)	$\tau'_{18}/\tau'_{9.7}$ (4)
IRAS 04074–2801	3.0	1.2	0.40
IRAS 05020–2941	2.4	0.9	0.38
IRAS 13106–0922	2.0	1.2	0.60
IRAS 14121–0126	1.3
IRAS 21477+0502	0.8
IRAS 03209–0806	1.0
IRAS 10594+3818	1.0
IRAS 12447+3721	1.4	0.5	0.36
IRAS 14202+2615	0.7
IRAS 15043+5754	1.4	0.7	0.50
IRAS 22088–1831	2.6	1.0	0.38
IRAS 02480–3745	1.4	0.6	0.43
IRAS 08591+5248	1.0
IRAS 02021–2103	1.4	0.4	0.29
IRAS 08474+1813	2.0	1.0	0.50
IRAS 14197+0813	0.8
IRAS 14485–2434	1.2

NOTE. — Col.(1): Object name. Col.(2): $\tau'_{9.7}$ is the optical depth of the 9.7 μm silicate dust absorption feature, plotted against a power-law continuum, shown as dotted lines in Figure 1. Col.(3): τ'_{18} is the optical depth of the 18 μm silicate dust absorption feature, plotted against a power-law continuum, shown as dotted lines in Figure 1. Col.(4): $\tau'_{18}/\tau'_{9.7}$ ratio for ULIRGs with clearly detectable 18 μm silicate absorption. The uncertainty with $\sim 10\%$ may be present.

TABLE 5
ICE ABSORPTION FEATURE

Object (1)	$\tau_{6.0}$ (2)
IRAS 04074–2801	0.3
IRAS 05020–2941	0.4
IRAS 13106–0922	1.0
IRAS 14121–0126	0.8
IRAS 21477+0502	0.6
IRAS 22088–1831	0.5
IRAS 02480–3745	0.9
IRAS 08591+5248	0.5
IRAS 14485–2434	0.3

NOTE. — Col.(1): Object name. Col.(2): Optical depth of the 6.0 μm H₂O ice absorption feature for clearly detected sources. The uncertainty with ~ 0.1 may be present.

TABLE 6
BURIED AGN SIGNATURES

Object (1)	EW _{6.2PAH} (2)	EW _{11.3PAH} (3)	$\tau'_{9.7}$ (4)	Total (5)
IRAS 04074–2801	○	X	○	○
IRAS 05020–2941	○	X	○	○
IRAS 13106–0922	○	X	○	○
IRAS 14121–0126	X	X	X	X
IRAS 21477+0502	X	○	X	○
IRAS 03209–0806	X	X	X	X
IRAS 10594+3818	X	X	X	X
IRAS 12447+3721	X	X	X	X
IRAS 14202+2615	○	X	X	○
IRAS 15043+5754	X	X	X	X
IRAS 22088–1831	○	○	○	○
IRAS 02480–3745	X	X	X	X
IRAS 08591+5248	X	X	X	X
IRAS 02021–2103	X	X	X	X
IRAS 08474+1813	○	X	○	○
IRAS 14197+0813	X	X	X	X
IRAS 14485–2434	○	X	X	○

NOTE. — Col.(1): Object name. Col.(2): Buried AGN signatures based on the low equivalent width of the 6.2 μm PAH emission ($\text{EW}_{6.2\text{PAH}} < 180 \text{ nm}$) (§5.2.1). ○: present. X: none. Col.(3): Buried AGN signatures based on the low equivalent width of the 11.3 μm PAH emission ($\text{EW}_{11.3\text{PAH}} < 200 \text{ nm}$) (§5.2.1). ○: present. X: none. Col.(4): Buried AGN signatures based on the large $\tau'_{9.7}$ value (≥ 2) (§5.2.2). ○: present. X: none. Col.(5): Buried AGN signatures from combined methods in Cols. (2)–(4). ○: strong. X: none.

TABLE 7
LUMINOSITIES OF BURIED AGNs AFTER EXTINCTION-CORRECTION AND
MODESTLY-OBSCURED STARBURSTS

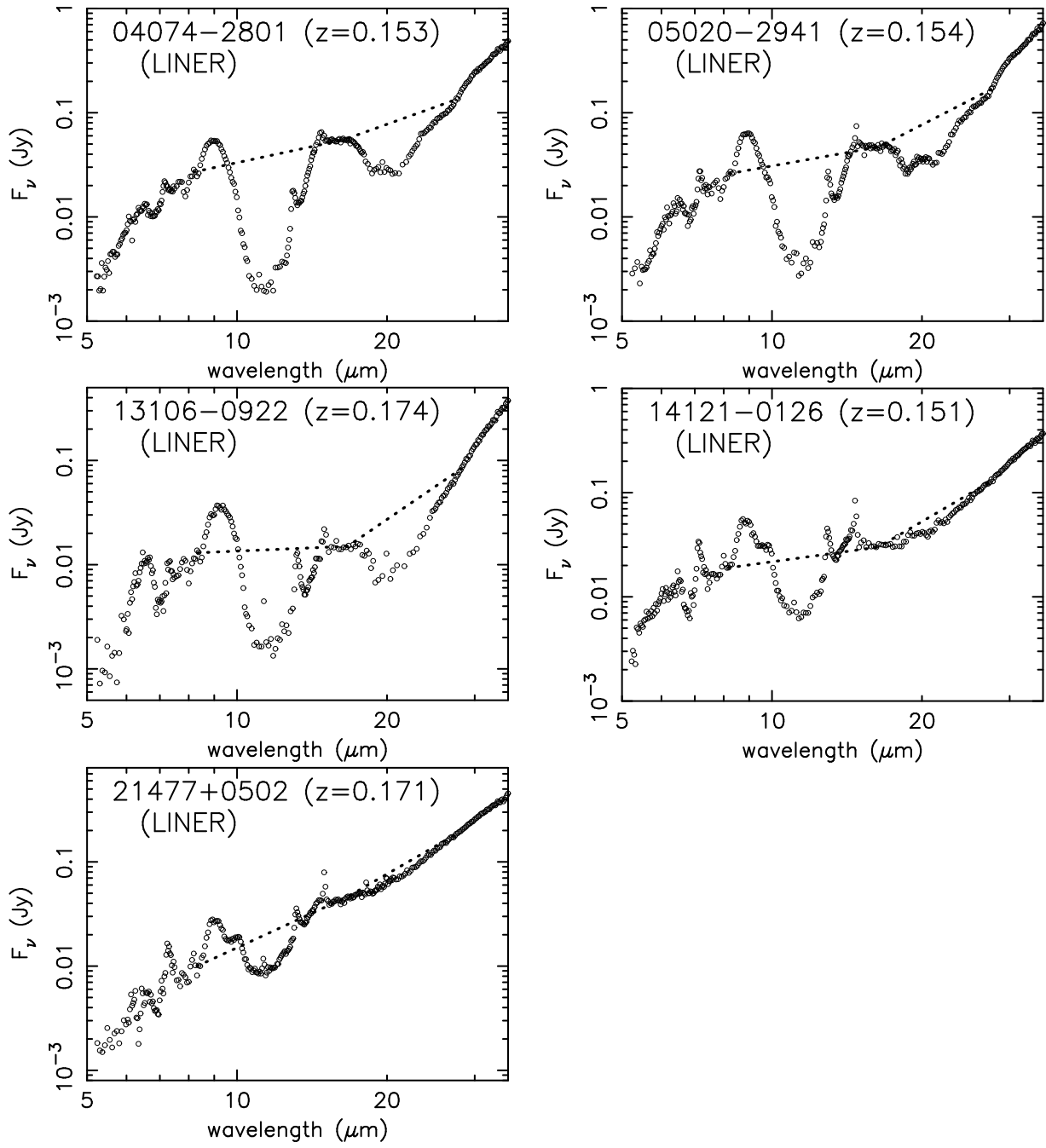
Object (1)	L(AGN) $10^{45} [\text{ergs s}^{-1}]$ (2)	L(SB-6.2PAH) $10^{45} [\text{ergs s}^{-1}]$ (3)	L(SB-11.3PAH) $10^{45} [\text{ergs s}^{-1}]$ (4)	L _{IR} $10^{45} [\text{ergs s}^{-1}]$ (5)
IRAS 04074–2801	2	1	2	6
IRAS 05020–2941	1.5	2	3	8
IRAS 13106–0922	1	1	2.5	8
IRAS 14202+2615	1	5.5	9.5	10
IRAS 22088–1831	1.5	1	1.5	10
IRAS 08474+1813	0.3	0.7	1	5
IRAS 14485–2434	1	2	5	5

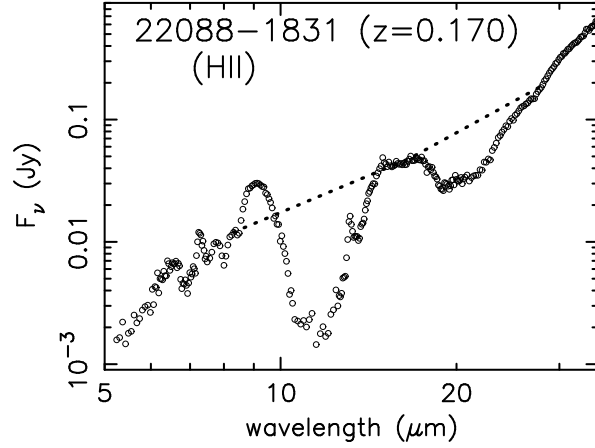
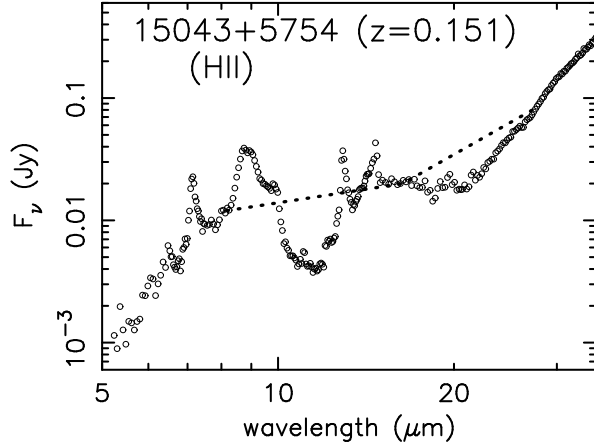
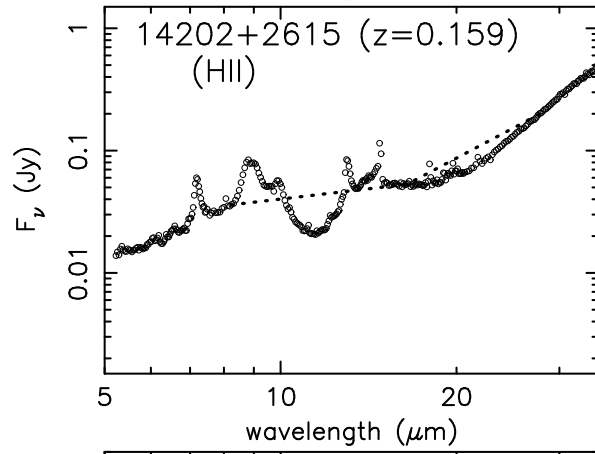
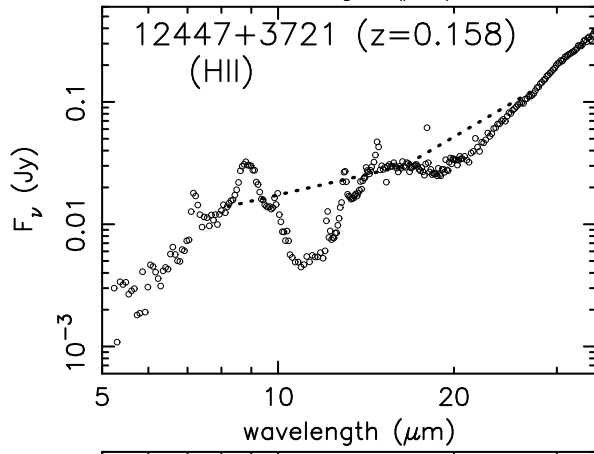
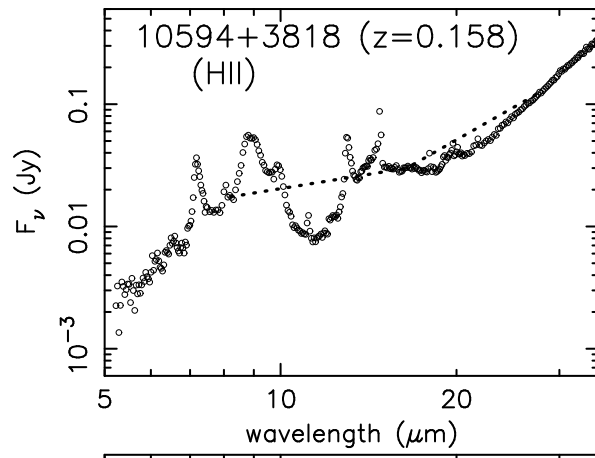
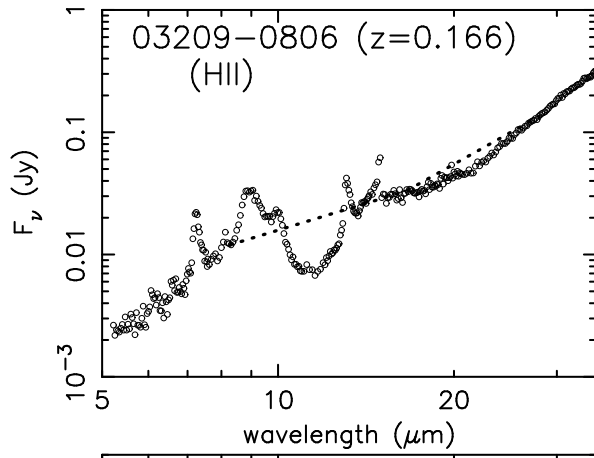
NOTE. — Col.(1): Object name. Col.(2): Extinction-corrected intrinsic luminosity of a buried AGN in units of $10^{45} [\text{ergs s}^{-1}]$. Col.(3): Infrared (8–1000 μm) luminosity of modestly-obscured ($A_V < 20 \text{ mag}$) starbursts, estimated from the 6.2 μm PAH emission luminosity ($L_{6.2\text{PAH}}$) and $L_{6.2\text{PAH}}/L_{\text{IR}} = 3.4 \times 10^{-3}$ (Peeters et al. 2004), in units of $10^{45} [\text{ergs s}^{-1}]$. Col.(4): Infrared (8–1000 μm) luminosity of modestly-obscured ($A_V < 20 \text{ mag}$) starbursts, estimated from the 11.3 μm PAH emission luminosity ($L_{11.3\text{PAH}}$) and $L_{11.3\text{PAH}}/L_{\text{IR}} = 1.4 \times 10^{-3}$ (Soifer et al. 2002), in units of $10^{45} [\text{ergs s}^{-1}]$. Col.(5): Observed infrared luminosity in units of $10^{45} [\text{ergs s}^{-1}]$.

TABLE 8
BURIED AGN FRACTION IN ULIRGS

Optical classification (1)	Sub-category (2)	number of sources (3)	Buried AGNs (4)
non-Seyfert	total	85	37 (44%)
	$L_{\text{IR}} < 10^{12.3} L_{\odot}$	54	15 (28%)
	$L_{\text{IR}} \geq 10^{12.3} L_{\odot}$	31	22 (71%)
	$z \leq 0.15$	52	18 (35%)
	$z > 0.15$	33	19 (58%)
LINER	total	43	21 (49%)
	$L_{\text{IR}} < 10^{12.3} L_{\odot}$	25	9 (36%)
	$L_{\text{IR}} \geq 10^{12.3} L_{\odot}$	18	12 (67%)
	$z \leq 0.15$	28	10 (36%)
	$z > 0.15$	15	11 (73%)
HII-region	total	32	12 (38%)
	$L_{\text{IR}} < 10^{12.3} L_{\odot}$	22	4 (18%)
	$L_{\text{IR}} \geq 10^{12.3} L_{\odot}$	10	8 (80%)
	$z \leq 0.15$	20	6 (30%)
	$z > 0.15$	12	6 (50%)
Unclassified	total	10	4 (40%)
	$L_{\text{IR}} < 10^{12.3} L_{\odot}$	7	2 (29%)
	$L_{\text{IR}} \geq 10^{12.3} L_{\odot}$	3	2 (67%)
	$z \leq 0.15$	4	2 (50%)
	$z > 0.15$	6	2 (33%)

NOTE. — Col.(1): Optical classification. Col.(2): Sub-category of ULIRGs. Whether $10^{12} L_{\odot} \leq L_{\text{IR}} < 10^{12.3} L_{\odot}$ or $L_{\text{IR}} \geq 10^{12.3} L_{\odot}$, and whether $z \leq 0.15$ or $z > 0.15$. Col.(3): Number of sources in each sub-category. Col.(4): Number and fraction of ULIRGs with strong buried AGN signatures in each sub-category (Imanishi et al. 2007; Imanishi 2009, this paper).





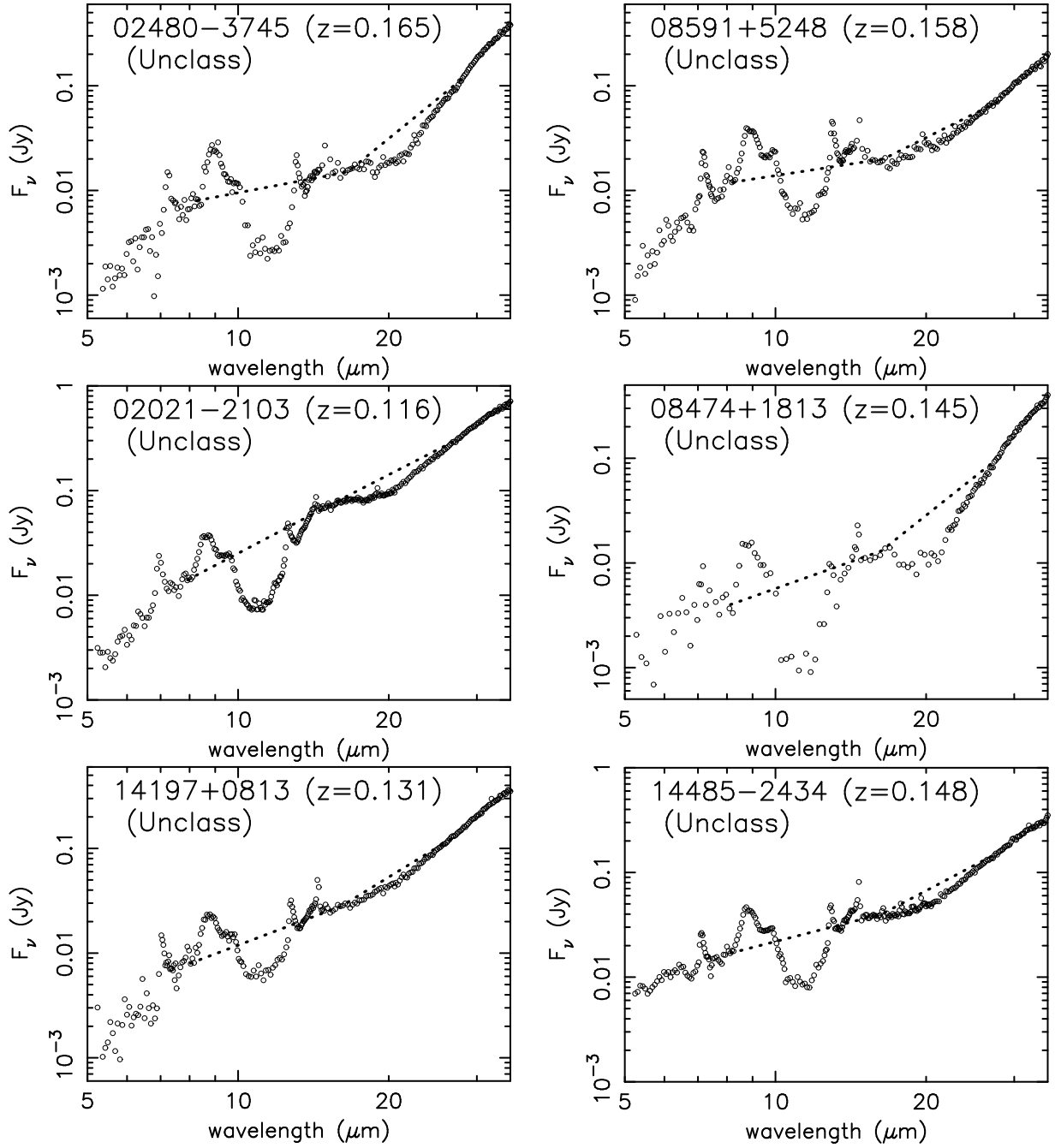
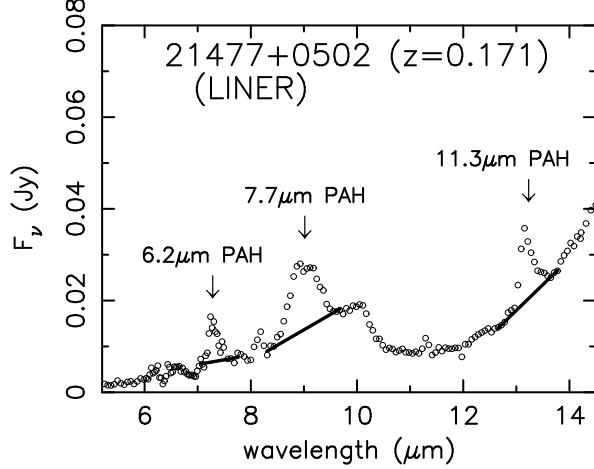
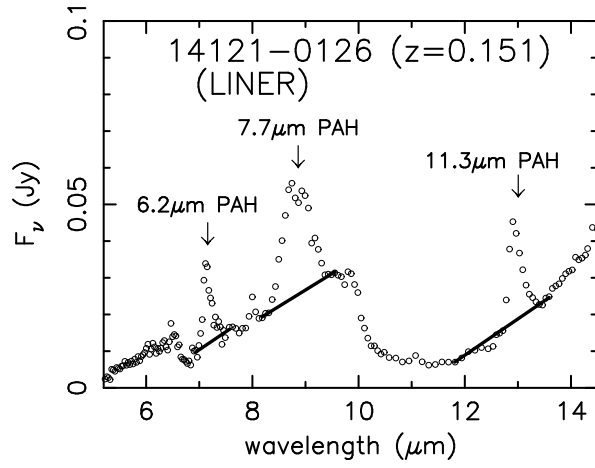
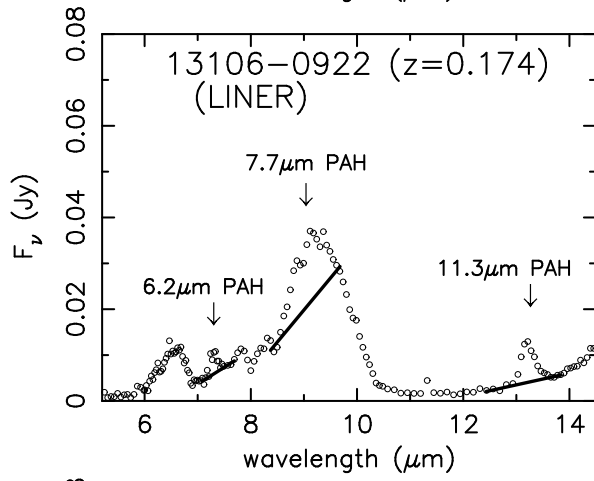
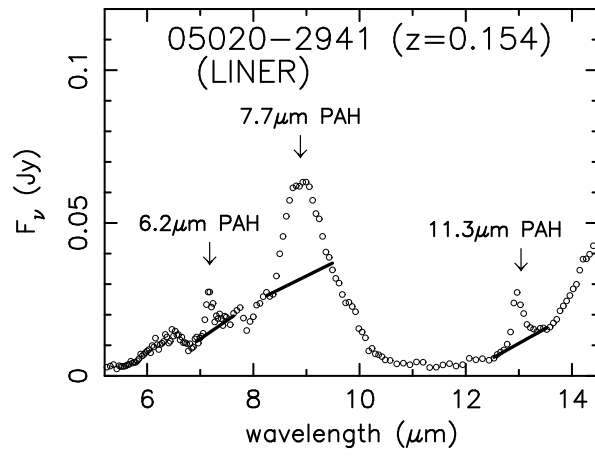
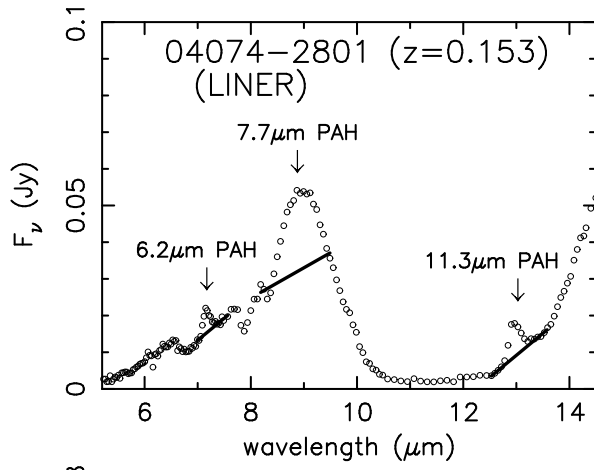
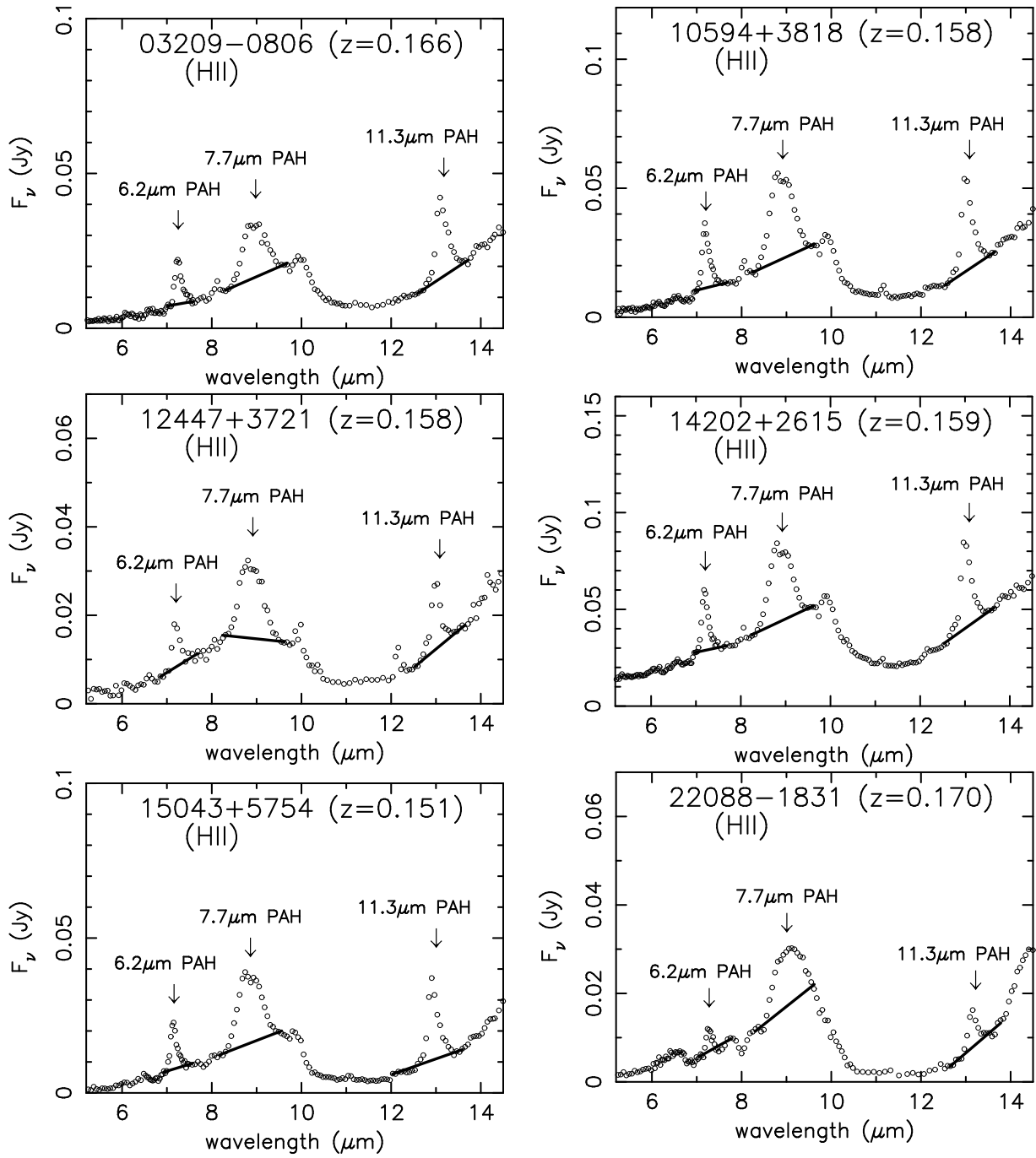


FIG. 1.— Infrared 5–35 μm spectra of optically non-Seyfert ULIRGs, taken with *Spitzer* IRS. The abscissa and ordinate are, respectively, the observed wavelength in μm and the flux F_ν in Jy, both plotted in a decimal logarithmic scale. For all objects, the ratio of the uppermost to the lowermost scale in the ordinate is fixed as a factor of 1000, to illustrate the variation of the overall spectral energy distribution. Dotted line: power-law continuum determined from data points at $\lambda_{\text{rest}} = 7.1 \mu\text{m}$ and $14.2 \mu\text{m}$ (in the rest frame) for the $9.7 \mu\text{m}$ silicate dust absorption feature, and at $\lambda_{\text{rest}} = 14.2 \mu\text{m}$ and $24 \mu\text{m}$ for the $18 \mu\text{m}$ silicate dust absorption feature (see §4.2).





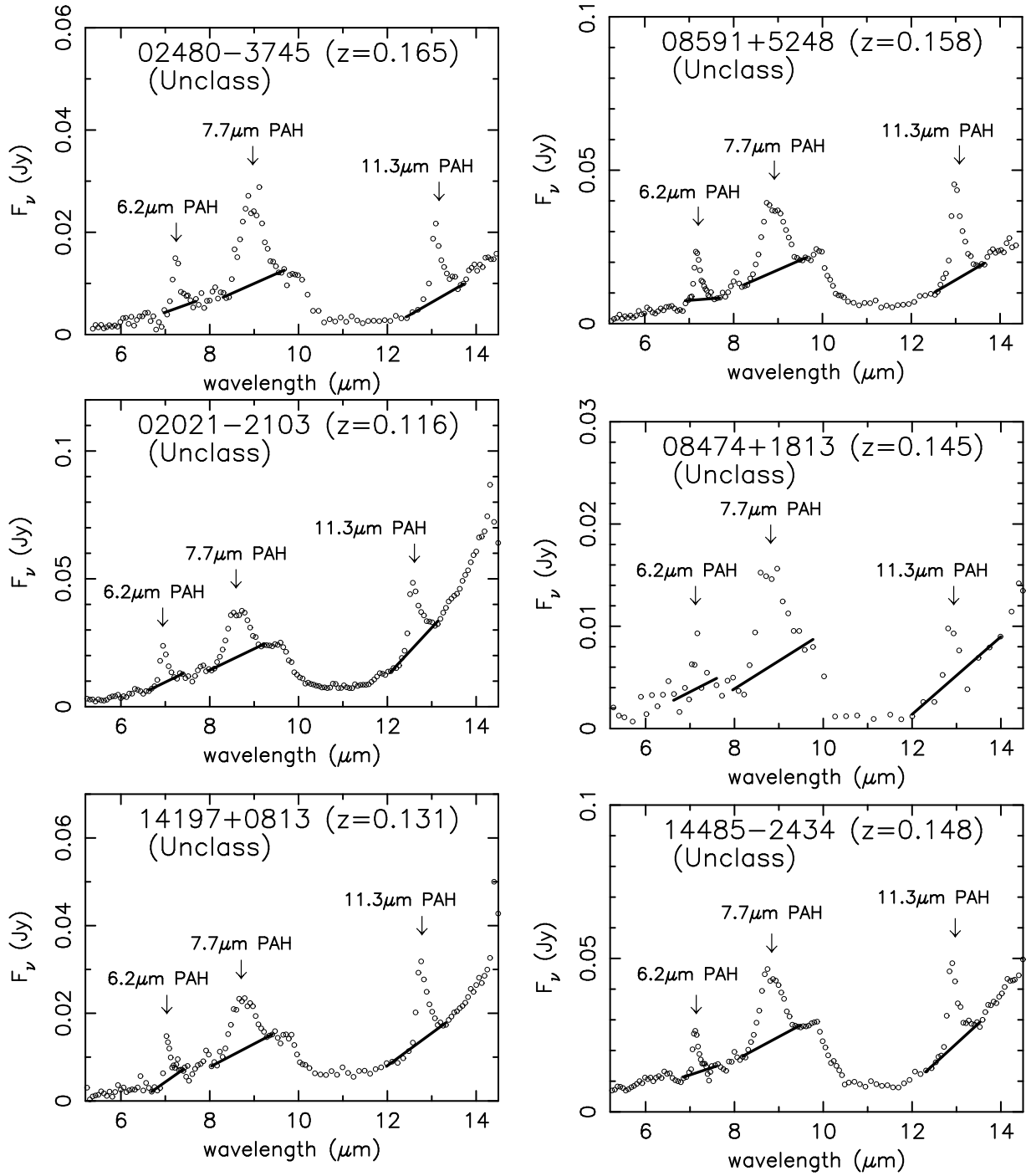
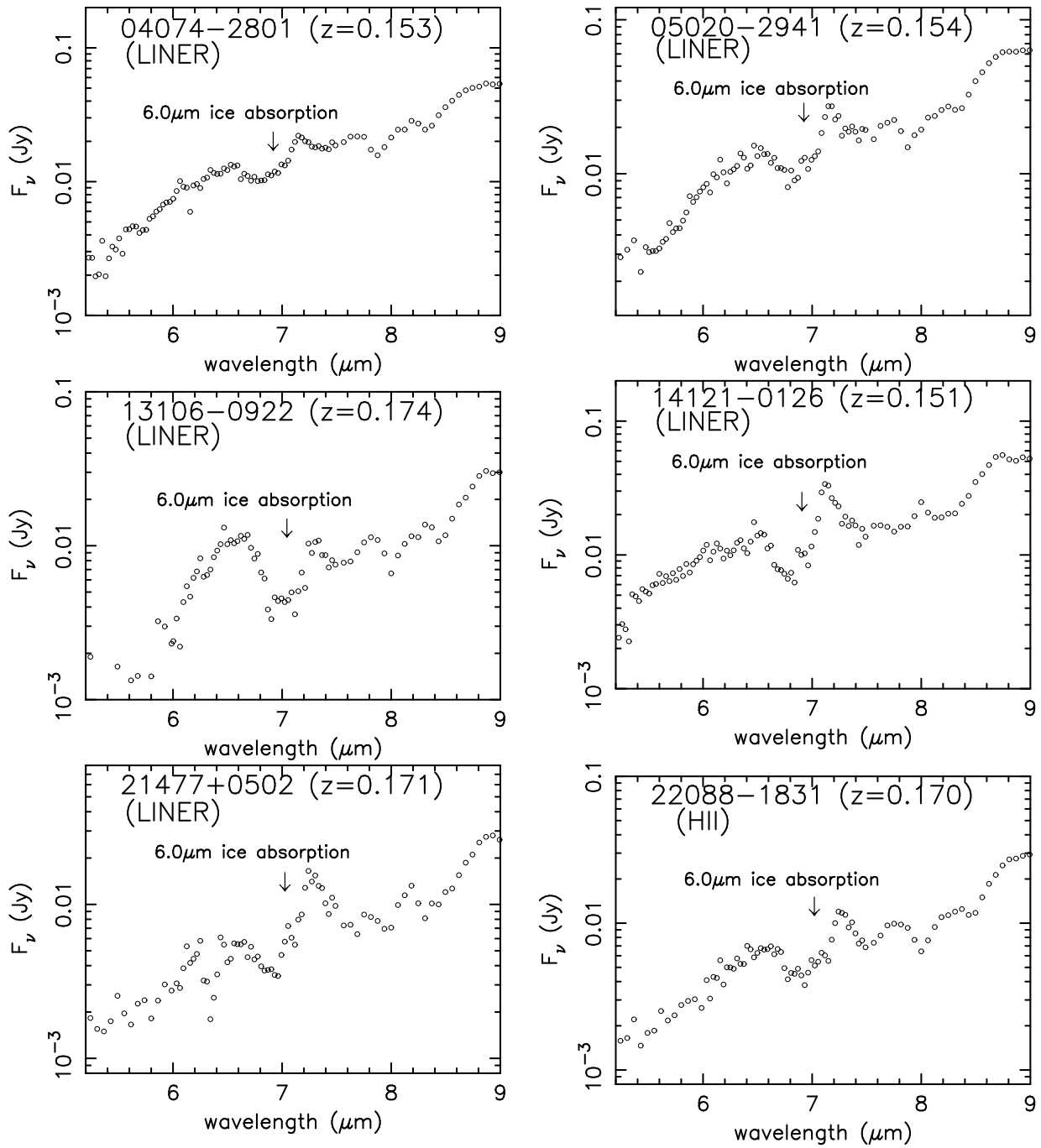


FIG. 2.— *Spitzer* IRS spectra of ULIRGs at $\lambda_{\text{obs}} = 5.2\text{--}14.5 \mu\text{m}$, for investigating the PAH emission in detail. The abscissa and ordinate are, respectively, the observed wavelength in μm and the flux in Jy, both plotted in a linear scale. The expected wavelengths of the 6.2 μm , 7.7 μm , and 11.3 μm PAH emission features are indicated as down arrows with labels. The solid lines are the adopted linear continuum levels for estimating the strength of the PAH emission (see §4.1).



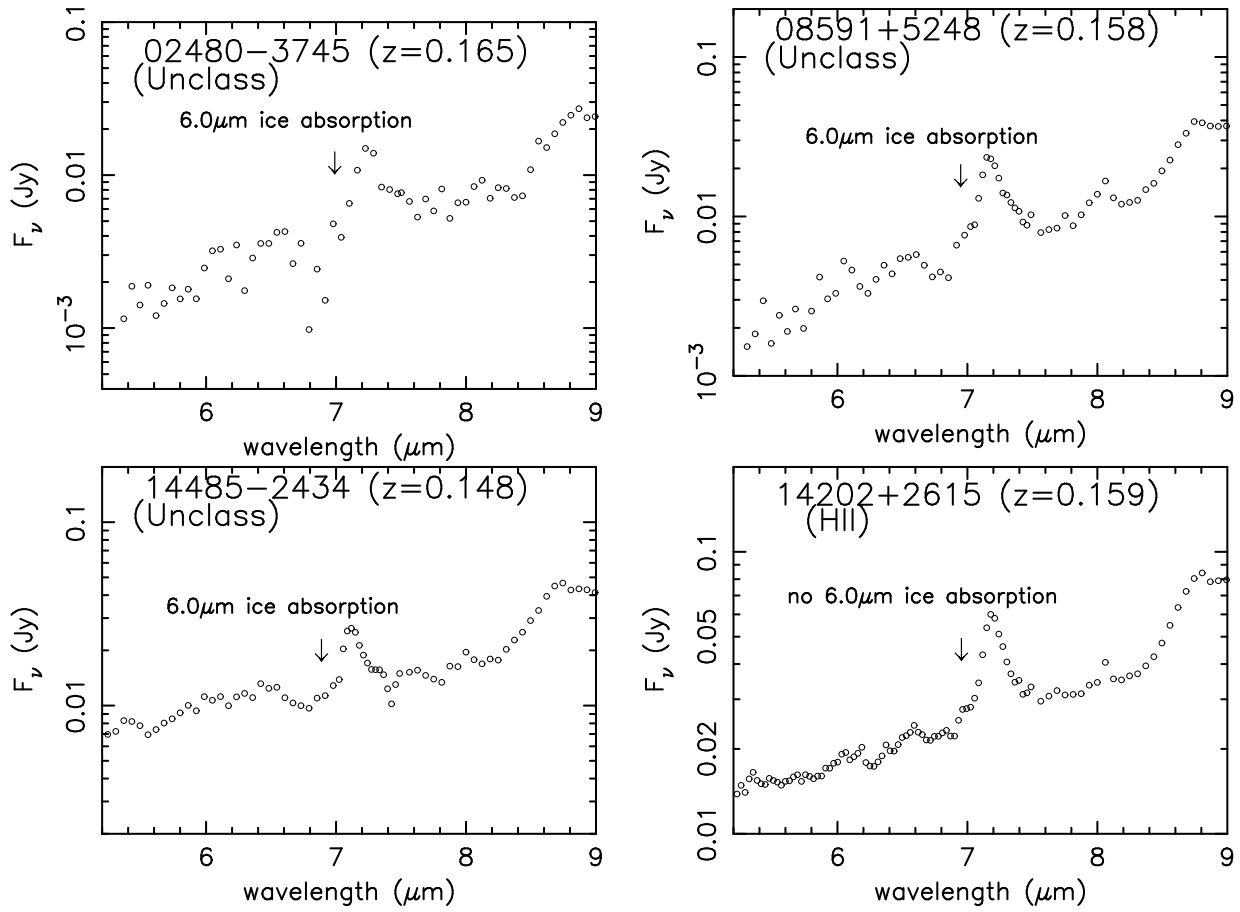


FIG. 3.— *Spitzer* IRS spectra at $\lambda_{\text{obs}} = 5.2\text{--}9\ \mu\text{m}$ for ULIRGs displaying clear $6.0\ \mu\text{m}$ H_2O ice absorption features (marked with “ $6.0\ \mu\text{m}$ ice absorption” in the first nine plots). The spectrum of IRAS 14202+2615, marked “no $6.0\ \mu\text{m}$ ice absorption”, is shown as an example of undetected ice absorption. The abscissa is the observed wavelength in μm plotted in a linear scale, and the ordinate is the flux in Jy plotted in a decimal logarithmic scale.

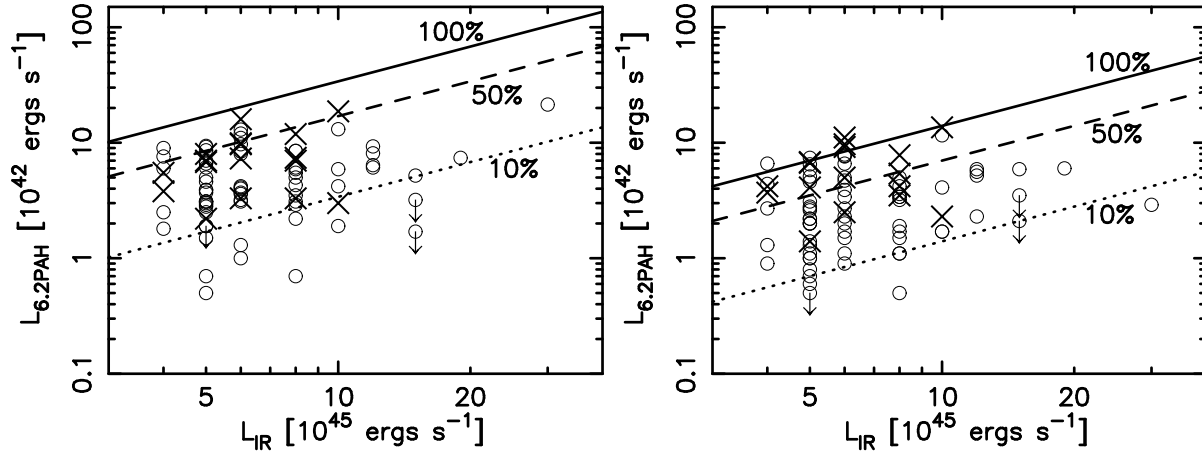


FIG. 4.— Comparison of the 6.2 μm (Left) and 11.3 μm (Right) PAH luminosities with the infrared luminosities. Optically non-Seyfert ULIRGs that were newly studied in this paper are plotted with “X” symbols. Open circles represent sources studied in previously published papers (Imanishi et al. 2007; Imanishi 2009). The solid lines indicate the canonical PAH to infrared luminosity ratios found in modestly obscured starburst galaxies (see §5.1). Specifically, on the solid lines, 100% of the infrared luminosity can be reproduced from the detected modestly obscured starburst activity. The dashed and dotted lines represent 50% and 10% of the ratios.

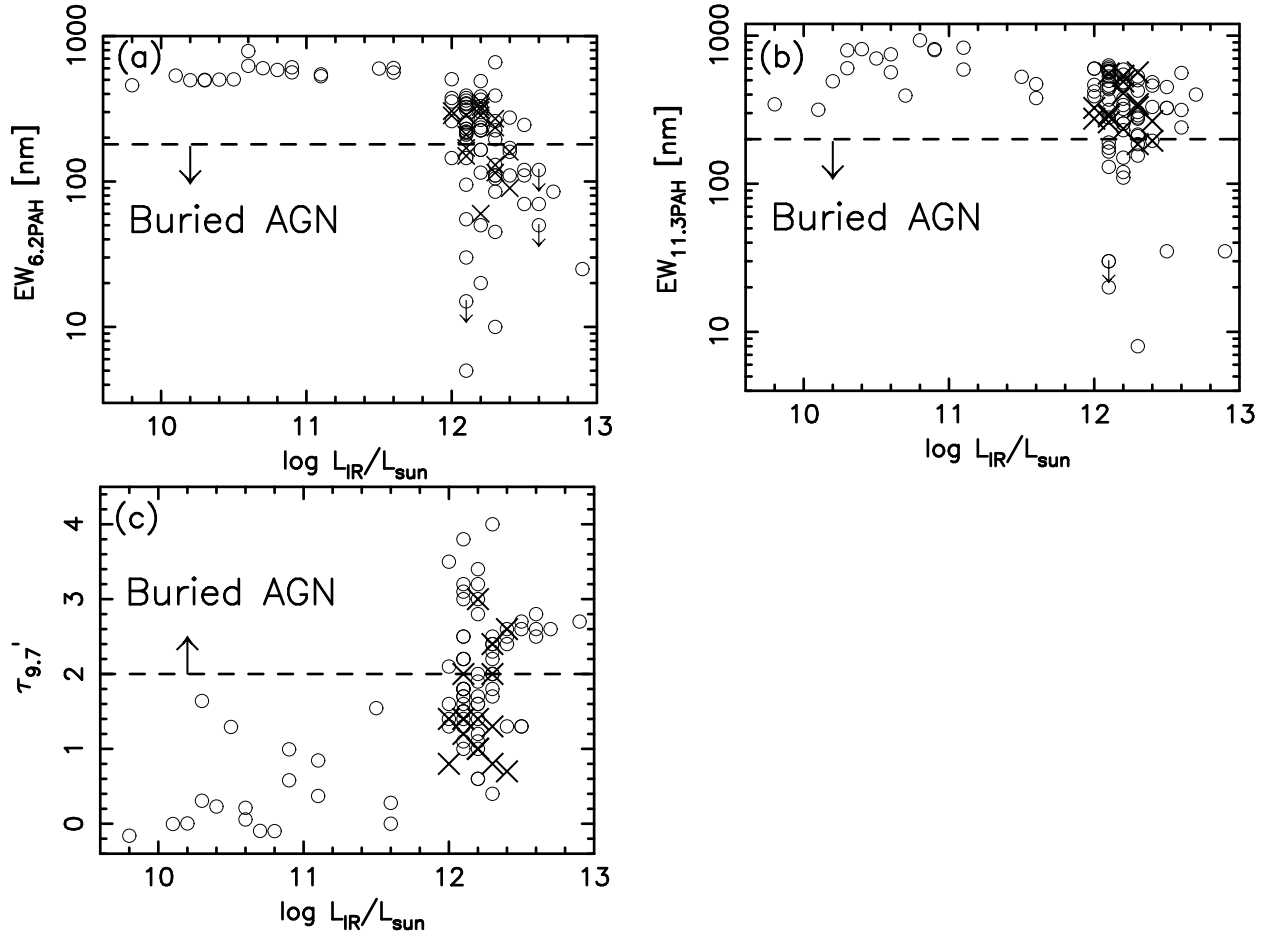


FIG. 5.— Distribution of (a) $EW_{6.2\text{PAH}}$, (b) $EW_{11.3\text{PAH}}$, and (c) $\tau'_{9.7}$, as a function of galaxy infrared luminosity. Optically non-Seyfert ULIRGs that were newly studied in this paper are plotted with “X” symbols. Open circles represent sources studied in previously published papers (Imanishi et al. 2007; Imanishi 2009; Brandl et al. 2006). The horizontal dashed lines indicate the threshold for buried AGN candidates (§5.2.1 and 5.2.2). For the plots (a) and (b), Desai et al. (2007) found similar trends for optically non-Seyfert ULIRGs, with the abscissa of 24 μm luminosity.

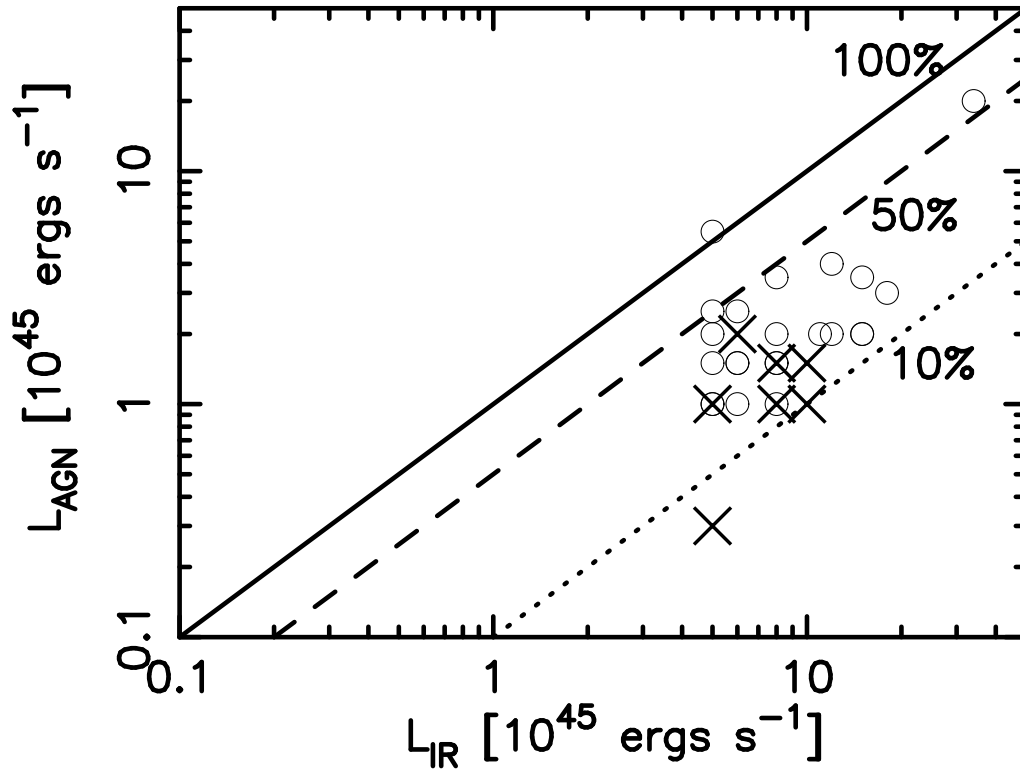


FIG. 6.— Comparison of the intrinsic buried AGN luminosity and observed infrared luminosity for selected ULIRGs with strong buried AGN signatures in their spectra (i.e., PAH equivalent widths are particularly low and the intrinsic AGN luminosities can be estimated with small ambiguities). Optically non-Seyfert ULIRGs that were newly studied in this paper are plotted with “X” symbols. Open circles represent sources studied in previously published papers (Imanishi et al. 2007; Imanishi 2009). The solid line indicates that the buried AGN luminosity equals the infrared luminosity. In other words, the observed infrared luminosity can be fully accounted for with a buried AGN. The dashed and dotted lines respectively indicate that 50% and 10% of the infrared luminosity can be explained by a buried AGN.

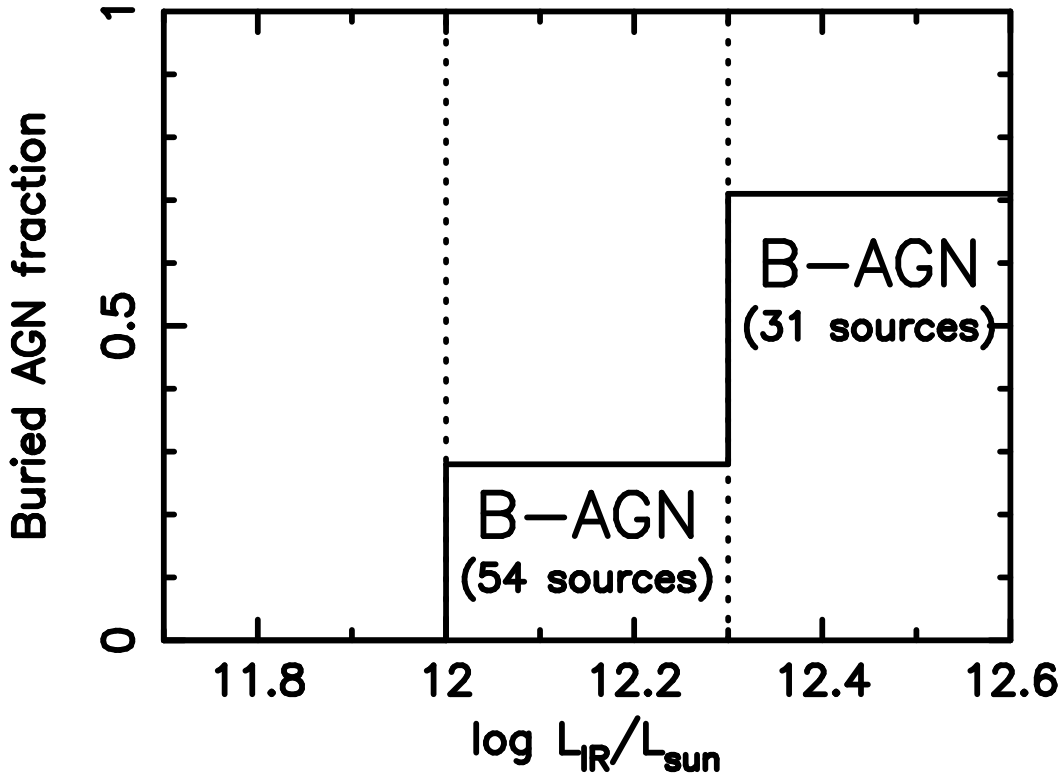


FIG. 7.— Fraction of sources with strong buried AGN signatures as a function of galaxy infrared luminosity. For ULIRGs ($L_{\text{IR}} \geq 10^{12} L_{\odot}$), the fraction is derived from the combination of Imanishi et al. (2007), Imanishi (2009) and this paper. The total number of sources is 54 for ULIRGs with $10^{12} L_{\odot} \leq L_{\text{IR}} < 10^{12.3} L_{\odot}$, and 31 for those with $L_{\text{IR}} \geq 10^{12.3} L_{\odot}$. For galaxies with $L_{\text{IR}} < 10^{12} L_{\odot}$, the fraction is obtained from the limited sample of 18 galaxies studied in Brandl et al. (2006), and does not necessarily imply that no buried AGNs are present. Although the sample is not statistically complete at $L_{\text{IR}} < 10^{12} L_{\odot}$, there should not be a strong bias, because the sources in this plot are essentially selected in the same way, based on the *IRAS* 60 μm fluxes.

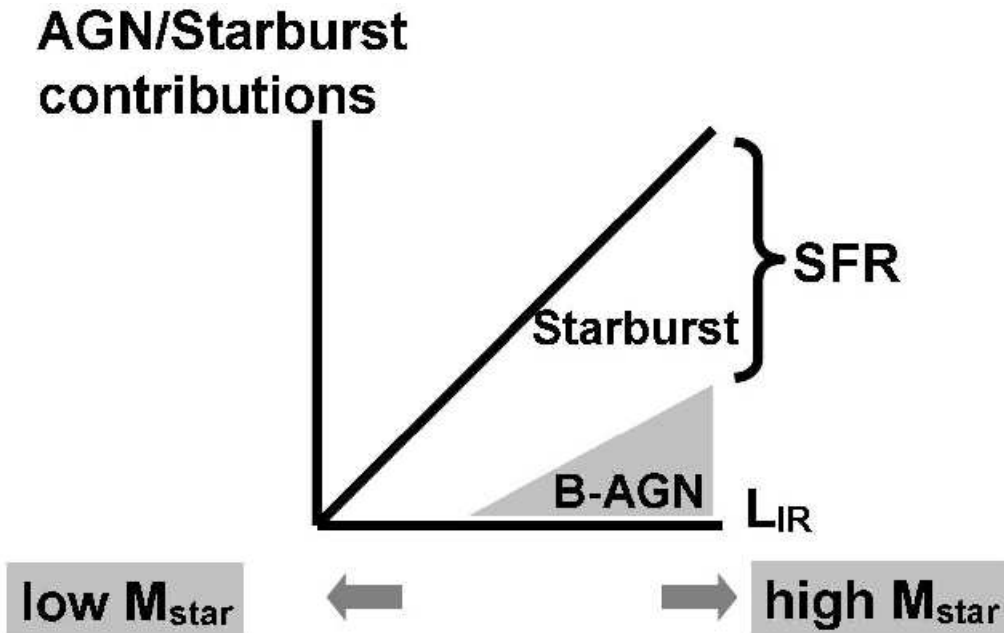


FIG. 8.— Schematic diagram of the energetic importance of buried AGNs (B-AGN) and starbursts as a function of galaxy infrared luminosity. Both the abscissa and ordinate are plotted in a linear scale. SFR stands for a star formation rate. In galaxies with higher infrared luminosities, the energetic importance of buried AGNs is *relatively* higher, and higher SFRs suggest that these galaxies will evolve into more massive galaxies with larger stellar masses.